Polymer Bulletin (2026) 83:441
https://doi.org/10.1007/s00289-026-06477-4

ORIGINAL PAPER

Antibacterial activity of PDDA-stabilized GO-AgNP nanocomposites

Badr-Edine Sadoq[1,3] · Youssef Elamine[2] · Inês Filipa Cabral Leal[3] · Adel Bouajaj[1] · Mohammed Reda Britel[1] · Amal Maurady[1,4] · Deborah M. Power[3,5]

Received: 30 December 2025 / Revised: 20 April 2026 / Accepted: 12 May 2026

Abstract

Graphene oxide (GO)-silver nanoparticle (AgNP) nanocomposites are widely studied for their antimicrobial synergy. In this study, the antibacterial activity of GO–AgNP nanocomposites prepared with poly(diallyldimethylammonium chloride) (PDDA) as a stabilizing linker was investigated. The composites were characterized by UV–Vis spectroscopy, FTIR, zeta potential analysis, XRD, TGA, and MP-AES. GO–PDDA–AgNPs exhibited a strong surface plasmon resonance band at ~420 nm, new C–H stretching bands at 2865–3012 cm^{-1} from PDDA, and a high positive zeta potential (+57.5 mV) compared to bare GO (–40 mV), confirming successful functionalization and improved colloidal stability. Antibacterial activity was evaluated against *E. coli* and *S. aureus* using disk diffusion assays, growth curves, and MIC determination. GO and AgNPs alone showed no inhibition at concentrations up to 20 µg/mL, whereas PDDA alone produced inhibition zones of 6–11.5 mm against *S. aureus* (2.5–100 µg/mL) and induced selective bacterial aggregation. The minimum inhibitory concentration (MIC) of PDDA was between 6.25 and 12.5 µg/mL for *S. aureus* and between 25 and 50 µg/mL for *E. coli*, indicating greater potency toward Gram-positive bacteria. The GO–PDDA–AgNP composite inhibited *S. aureus* with zones of 8.5–10 mm at 10–20 µg/mL, while no significant inhibition was observed for *E. coli* at the tested concentrations. Molecular docking simulations examining interactions between PDDA and quorum-sensing regulatory proteins AgrA in *S. aureus* and LsrR in *E. coli* predicted higher binding affinity to AgrA (–5.11 kcal/mol) than LsrR (–3.76 kcal/mol). While in vitro assays using a *Chromobacterium violaceum* CV026 biosensor showed no inhibition of AHL-mediated signalling, it should be noted that this model differs mechanistically from the Gram-positive *agr* system, leaving the predicted AgrA interaction as a potential target for future investigation. Ultimately, this study demonstrated that PDDA is the primary antibacterial component of the GO–PDDA–AgNP composite, exhibiting potent activity against Gram-positive bacteria through a mechanism involving selective bacterial aggregation.

Extended author information available on the last page of the article

Keywords GO-AgNP composites · Polymeric stabilizer · Functional nanomaterials.

Introduction

Advances in nanotechnology, particularly the ability to engineer nanomaterials with specific sizes and shapes, hold promise for the development of novel antibacterial agents. Noble metals [1] and metal oxide-based nanomaterials [2], such as Ag, Au, ZnO, TiO_2, Cu_2O nanoparticles (NPs), and their nanohybrids, have been extensively studied due to their potent antimicrobial properties [3–6]. Among these, silver nanoparticles (AgNPs) are promising because of their unique physical and chemical properties, their high surface-area-to-volume ratio, which enhances their interaction with microbial membranes [7].

AgNPs have proven effective against multidrug-resistant microorganisms where antibiotics have failed, demonstrating efficacy against both Gram-negative and Gram-positive bacteria. The actions of AgNPs are attributed to diverse mechanisms, including generation of reactive oxygen species (ROS), ion release, DNA damage, inhibition of protein synthesis, and modulation of microbial signal transduction pathways, ultimately leading to microbial cell death [4, 8, 9]. Beyond antibacterial effects, nanotechnology-based strategies, including AgNPs, have been explored for antiviral applications, acting at different levels of the complex viral invasion, replication, and immune evasion mechanisms [10]. Graphene oxide (GO)-based nanocomposites incorporating metal oxides such as ZnO, in common with AgNPs, have broad-spectrum antimicrobial activities against both Gram-positive and Gram-negative pathogens, including drug-resistant strains, which highlights the versatility of graphene-based platforms in combating microbial infections [11].

Despite the promise of AgNPs as antimicrobial agents, drawbacks to their use include their low stability in aqueous solutions, which induces spontaneous aggregation and reduces their surface area and antimicrobial activity [12, 13]. This limitation can be addressed by using GO as a dispersing carrier. GO, a single plane of carbon atoms arranged in a hexagonal lattice, with oxygen-containing groups (e.g., epoxy, hydroxyl, carboxyl), offers excellent hydrophilicity, defect sites, and colloidal stability in water [14–16]. Graphene-supported silver nanoparticle systems show consistent improvements in activity compared to the individual components, and reduce the minimum inhibitory concentration (MIC) of phosphomolybdic acid (PMo) from 3920 µg/mL to 512 µg/mL when combined with reduced GO (PMo/RGO), and the MIC is further reduced to 256 µg/mL with the addition of AgNP [17]. Green-synthesized rGO/AgNP nanocomposites have further demonstrated that combining rGO with AgNPs improves stability and yields enhanced biological activity, including notable antitumor effects, underscoring the synergistic potential of such hybrid systems [18]. Moreover, optimization of synthesis conditions, including the silver nitrate concentration, pH, and temperature, is critical for maximizing the antimicrobial efficacy of rGO/AgNP nanocomposites, with optimized systems exhibiting superior performance against a range of clinically relevant pathogens [19].

To further enhance stability and function of metal NP complexes, polymers are often employed as linkers. Among these, poly(diallyldimethylammonium chloride) (PDDA) is attractive due to its permanent cationic charge, biocompatibility, and non-toxic profile [20, 21]. PDDA adsorbs onto the GO structure through its π-orbitals, thereby preserving the electronic structure of GO [22], and consequently its hydrophilicity, contributes to good chemical stability, and high mechanical strength. These properties make it an ideal platform for stabilizing AgNPs. The use of PDDA as a surface modifier in Ag/rGO systems has been demonstrated across diverse applications for instance, in functional textile fabrication, PDDA modification significantly improves the adhesion, uniformity, and overall performance of Ag/rGO coatings, resulting in nanocomposites with superior electrical, antistatic, and electromagnetic shielding properties [23]. Synthesis conditions also play a critical role in defining nanoparticle stability and functionality. Ultrasound-assisted methods, for instance, have been shown to greatly improve AgNP dispersion and enhance the electrical and rheological properties of colloidal systems [24]. Several studies have successfully used PDDA in the synthesis of GO-AgNP composites. Du et al. [25] synthesized GO-AgNP nanocomposites using PDDA as a linker through an interfacial electrostatic self-assembly method. GO (negative) was functionalized with PDDA (positive) via electrostatic interactions and resulted in the stable incorporation of AgNPs, and a stronger antiviral activity compared to AgNPs and GO alone. Similarly, Zhu et al. [26] demonstrated that GO-AgNP composites, assembled using PDDA as a linker, exhibited enhanced colloidal stability, photo-stability, and antibacterial activity against *E. coli*, and *B. subtilis*, compared to AgNPs alone.

Poly(diallyldimethylammonium chloride) has been extensively utilized in various nanomaterial systems beyond GO–AgNP composites. Its pronounced cationic charge facilitates its application in water purification, antimicrobial coatings, and as a stabilizing agent in nanoparticle formulations [27, 28]. Notably, PDDA itself possesses inherent antibacterial properties. For instance, Sanches et al., documented significant antimicrobial activity of free PDDA in comparison with PDDA immobilized in nanoparticles [29]. Furthermore, PDDA has been utilized in the functionalization of gold nanoparticles for biosensor platforms. Yu et al. showed that PDDA-capped AuNPs on graphene/multi-walled carbon nanotube composites provide a favourable surface for enzyme immobilization, allowing direct electron transfer for glucose detection [30]. More recently, PDDA has been employed as a functional linker in AuNP-rGO nanocomposites for electrochemical sensing applications, further confirming its versatility as a stabilizing and structurally directing agent across a range of nanomaterial fabrication contexts [31]. These findings underscore the role of PDDA not only as a stabilising agent but also as a bioactive polymer, providing the basis for understanding its contribution in GO-AgNP systems.

The successful incorporation of PDDA into the fabrication of GO-AgNP nanocomposites is typically confirmed by a high, positive zeta potential and enhanced colloidal stability [32]. This observation points to a relevant but underexplored aspect: the potential retention of PDDA's antimicrobial activity within such nanocomposites. Free PDDA is known to exhibit strong antibacterial effects, and previous work has shown that this activity may diminish when introduced into other systems, such as PMMA nanoparticles [29]. To the best of our knowledge, this aspect has not been explored in GO–AgNP-based composites, where PDDA serves as a linker and may influence the overall biological performance of the composite. In this context, the present study aimed to elucidate the specific contribution of PDDA to the antibacterial activity of GO-PDDA-Ag nanocomposites. To achieve this, GO-PDDA-AgNP nanocomposites were prepared and characterized using physicochemical techniques, including UV-Vis spectrophotometry, FTIR spectroscopy, size distribution analysis, polydispersity index, and zeta potential measurements. The antibacterial characteristics were analysed using qualitative (zone of inhibition) and quantitative (bacterial growth curve, MIC) methods with gram-negative (*E. coli*) and gram-positive (*S. aureus*) bacteria. To investigate the origin of the antimicrobial activity of PDDA, which possesses a high cationic charge, we tested the hypothesis that its mechanism of action may involve disruption of quorum-sensing (QS) pathways. Proteins from QS networks, that govern biofilm formation, virulence, and antibiotic resistance [33, 34] through autoinducers and their regulatory proteins [35, 36] were analysed by in silico molecular docking studies and in vitro assays with a *Chromobacterium violaceum* CV026 biosensor.

Materials and methods

Materials

A highly concentrated aqueous dispersion of graphene oxide (GO, 5 mg/mL, Carbon, ≥ 46%, Oxygen, ≤ 46%, and flake size of 0.5–5 µm) was purchased from the Graphene Supermarket (SKU-HCGO-W-175; Graphene Supermarket, New York, NY, USA). Silver nanoparticles (AgNPs) with a particle size of 40 nm (TEM) and a concentration of 0.02 mg/mL in an aqueous buffer containing sodium citrate as a stabilizer (product number 730785), were obtained from Sigma-Aldrich (Madrid, Spain). Poly(diallyldimethylammonium chloride) (PDDA), available as a 35% solution in water, was also purchased from Sigma-Aldrich.

Preparation of graphene oxide–silver nanoparticle nanohybrids (GO–PDDA-AgNPs)

GO–AgNP nanohybrids were prepared following the electrostatic self-assembly method described by Zhu et al. [26], with minor modifications. Specifically, commercially available AgNPs (40 nm, 0.02 mg/mL) were used in place of synthesized particles, and the GO–PDDA conjugate was prepared by mixing 1 mL of GO (4.0 mg/mL) with 0.8 mL of PDDA (10 mg/mL), adjusting the pH to 6.5 (NaOH: 1.0 M solution). The mixture was subjected to ultrasonic treatment (20 kHz, 130 W, Pulse 15:15, 80% amplitude) for 10 min and the excess PDDA was removed by three centrifugation steps of 13,000 rpm, for 10 min. The resulting GO–PDDA was mixed with 500 µL of AgNPs (0.02 mg/mL) using sonication (20 kHz, 130 W for 1 min). The resulting material was recovered by centrifugation (5,000 rpm, 1 min) and was redispersed in water for experiments (Fig. 1).

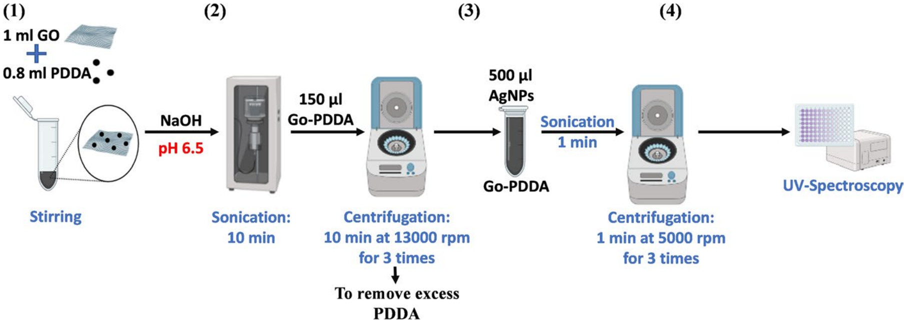

Fig. 1 A scheme illustrating the main steps for the preparation of Graphene Oxide–PDDA-Silver Nanoparticle Nanohybrids. The synthesis process of GO–PDDA-AgNP nanohybrids was achieved by mixing 1 mL of GO solution (4.0 mg/mL) with 0.8 mL of PDDA solution (10 mg/mL) and adjusting the pH to 6.5 using NaOH. After mixing, the reaction was exposed to ultrasound for 10 min in pulse mode (Pulse 15:15, amplitude 80%). Following sonication, the mixture was centrifuged at 13,000 rpm for 10 min to remove excess PDDA. The GO-PDDA product (150 µL) was mixed with AgNPs (500 µL, 0.02 mg/mL) and exposed to ultrasound for 1 min. The final mixture was centrifuged at 5,000 rpm for 3 min before use in subsequent experiments

To evaluate the effect of the PDDA concentration on the antibacterial activity of the nanocomposite, a second formulation was prepared using a diluted PDDA solution (1.25 µg/mL), a level at which PDDA alone exhibited no antibacterial effect. This control formulation, labelled GO-PDDA*-AgNPs, was synthesized following the same procedure used for the primary formulation.

Physicochemical characterization

The UV-visible absorption spectra of GO, PDDA, AgNPs, GO-PDDA-AgNPs and GO-PDDA*-AgNPs were measured using a BioTek spectrometer (Synergy 4 Hybrid, Model S4MLFTAD) in scanning mode across the wavelength range of 200–800 nm. The measurements were carried out using a UV-compatible 96-well plate with a concave bottom to ensure accurate absorbance readings. Each sample was analysed in triplicate to ensure reproducibility.

A Fourier transform infrared spectrometer (Nicolet iN10 MX FT-IR Microscope IR, Thermo Scientific, USA) was used to analyse the GO, AgNPs, GO-PDDA, GO-PDDA-AgNPs and GO-PDDA*-AgNPs. For analysis, each sample was transferred to a slide, which was introduced into the reading station of a micro-FTIR and FTIR spectra were captured in the attenuated total reflectance (ATR) mode with a wavenumber range of 700 to 4000 cm^{-1}. ATR-FTIR spectroscopy was used rather than transmission FTIR spectroscopy because the composite was analysed in its solid state and since the ATR component offers a cost-effective, relatively fast and nondestructive approach [37].

Nanoparticle size and the polydispersion index (PDI) were determined using dynamic light scattering (DLS), and the zeta potential was measured using laser Doppler anemometry (Zetasizer Nano ZS, Malvern Instruments, UK). To prepare the samples, 20 µL of GO, AgNPs, GO-PDDA, GO-PDDA-AgNPs and GO-PDDA*-AgNPs were diluted in 1 mL of ultrapure water (pH 6.5). All measurements were conducted at 25 °C, and three replicates were performed. All data were generated and acquired using the instrument software.

The change in mass of the NPs was determined by thermogravimetric analyses (TGA) using a PerkinElmer TGA 7 instrument over a temperature range of 30–700 °C at a heating rate of 10 °C.min^{-1} under a continuous nitrogen flow. The mass scale was calibrated using a certified 100 mg reference weight, and the temperature calibration was carried out using the Curie transition temperatures of alumel (427.35 K) and high-purity nickel (628.45 K), in accordance with PerkinElmer standard reference materials. To assess the internal atomic structure, phase purity, crystallinity, and crystal size of NPs, powder X-ray diffraction (XRD) patterns were obtained using a Bruker D8 Advance diffractometer equipped with Ni-filtered Cu Kα radiation and a 1D LynxEye detector and scanning over the 2θ range of 5°-60°.

The quantification of silver within the GO-PDDA-AgNP composite was conducted by filtration of the nanocomposite reaction products using a 13 mm PTFE hydrophobic syringe filter (0.2 µm, Labfil, Cat. No. C0000610). To determine the amount of free AgNPs not integrated within the nanocomposite the filtrate was measured using a Microwave Plasma–Atomic Emission Spectrometer (MP-AES, Agilent 4200) at an analytical wavelength of 328.068 nm. Calibration standards, ranging from 0.039 µg/mL to 10 µg/mL, were prepared from a 1000 µg/mL Ag stock solution (Merck).

Evaluation of nanocomposite antibacterial activity

In the present study the antibacterial activity of the nanocomposites and individual reagents used for their fabrication (GO-PDDA, and GO-PDDA-AgNPs, PDDA) were determined using gram-negative (*Escherichia coli*, *E. coli* DSM 1077) and gram-positive (*Staphylococcus aureus*, *S. aureus* C48) bacteria. The antibacterial activity of the nanocomposites and PDDA alone was investigated using the disk diffusion method and the growth curve method [38, 39]. Before analysis the bacterial strains were cultured on Mueller-Hinton (MH) agar plates in an incubator overnight at 37 °C. A single colony was inoculated into 5 mL of MH broth and grown overnight at 37 °C under constant agitation (150 rpm) in an incubator. The bacterial cultures prepared were then used in disk diffusion and growth curve assays. Control assays were also performed to assess the intrinsic antibacterial activity of GO and AgNPs. GO was tested at concentrations up to 4.0 mg/mL, corresponding to that of the stock solution used in the synthesis, and AgNPs (20 µg/mL) were tested at concentrations higher than those present in the final nanocomposite.

Disk Diffusion Method: The bacterial inoculum of *E. coli* or *S. aureus* was adjusted to an optical density ($OD_{600\ nm}$) of 0.3. Using a sterilized cotton bud, the cultures were swabbed evenly on the MH agar plates. Subsequently, a fixed volume of 10 µL of an aqueous suspension of AgNPs, GO, PDDA, and GO-PDDA-Ag, nanocomposite at concentrations of, 10, 15 and 20 µg/mL, were dropped onto the plates. For PDDA, serial dilutions with the following concentrations: 100 µg/mL, 10 µg/mL, 5 µg/mL, 2.5 µg/mL and 1.25 µg/mL were all tested. Additionally, 10 µL of PBS was used as a negative control. The plates were left for several minutes to allow the test suspensions to soak in and were then incubated overnight at 37 °C in an incubator. The inhibitory effect of the test suspensions on the bacterial growth was determined by measuring the diameter of the inhibition zone (mm). All experiments were carried out in triplicate.

Bacterial Growth Inhibition Assay: The overnight cultures of *E. coli* and *S. aureus* were diluted to 1:5 in MH broth, and the $OD_{600\ nm}$ was adjusted to 0.1 to standardise the initial bacterial concentration. Then, 20 µL of this adjusted culture was used to inoculate 96-well plates. Each well contained 170 µL of MH broth and 10 µL of an aqueous suspension of AgNPs, GO, and GO-PDDA-Ag nanocomposite at concentrations of 10, 15, or 20 µg/mL. To test the antibacterial activity of PDDA, bacterial growth was assessed using the same set-up outlined above but using 10 µL and testing serial dilutions at 100 µg/mL, 10 µg/mL, 5 µg/mL, 2.5 µg/mL and 1.25 µg/mL. All bacterial growth inhibition assays included bacteria in MH broth without the addition of nanoparticles (positive control to monitor growth) or uninoculated MH broth to confirm the absence of bacterial contamination. Bacterial growth inhibition assays were carried out in triplicate wells (technical replicates) for each treatment, and the assay was repeated in three independent trials. Bacterial growth was monitored hourly across fourteen hours by measuring OD_{600nm} using a Synergy Neo2 Hybrid Multi-Mode Multiplate Reader (Biotech, USA).

Resazurin microdilution assay for minimum inhibitory concentration determination: The minimum inhibitory concentration (MIC) of PDDA against *E. coli* and *S. aureus* was assessed utilizing the resazurin microdilution method [40] in a sterile 96-well microplate (Sarstedt, Germany). Overnight bacterial cultures were diluted at a ratio of 1:5 in MH broth (MHB), and the OD_{600} nm was adjusted to 0.1 to standardize the initial bacterial concentration. Each well contained 170 µL of MHB, 10 µL of PDDA solution at the desired concentration, and 20 µL of the bacterial inoculum. Serial dilutions of PDDA were prepared to obtain final concentrations of 100, 50, 25, 12.5, 6.25 and 3.12 µg/mL. Control wells included *E. coli* or *S. aureus* without PDDA, or MHB alone as a sterility control. Additionally, three wells containing MHB with PDDA but without bacterial inoculum were included to verify the absence of any interference from PDDA in the assay. Plates were incubated at 37 °C for 24 h, followed by the addition of 10 µL of resazurin solution (AlamarBlue™, Invitrogen™, Cat. No. DAL1025) to each well. The plates were then incubated for an additional 2–4 h until color development. A change in colour from blue to pink indicated bacterial growth, whereas the persistence of the blue color indicated growth inhibition [40]. The MIC was defined as the lowest concentration of PDDA that prevented the color change. Each assay was performed in triplicate, and two independent experiments were conducted to confirm the reproducibility of the assay.

Study of bacterial aggregation The results of the *S. aureus* growth curves in the presence of PDDA were indicative of bacterial aggregation. This was confirmed by placing two microliters of each of the test samples on a glass slide and staining them with Gram stain. The stained cells were then captured in black-and-white digital images using a Leica DM IL microscope coupled to a Visicam PRO 20 C digital camera.

Molecular docking analysis

Molecular docking studies were conducted to complement the in vitro experimental results and identify the putative source of the antibacterial activity. The studies modelled the interactions between PDDA and key bacterial proteins. Specifically, QS-regulated proteins and novel targets of emerging anti-infective strategies, the transcription factors AgrA in *S. aureus* [41] and LsrR in *E. coli* were analysed [42]. Additionally, ciprofloxacin (Compound CID: 2764), a known antibiotic, was included as a reference ligand in the modelling studies and to provide a benchmark for antibacterial efficacy and a point of comparison for the binding interactions and affinities of PDDA.

The docking simulations performed using AutodockTools software [43], provided insight into the molecular mechanisms underlying the observed antimicrobial effects. The 3D molecular structures of the two most vital and positively identified bacterial quorum-sensing proteins were obtained from the Protein Data Bank (PDB) at https://www.rcsb.org under the accession numbers *S. aureus* AgrA (PDB ID: 4G4K) and *E. coli* LsrR (PDB ID: 4L5J) [42]. The protein structures were prepared for analysis as follows [44]: (i) removal of water molecules and co-crystal ligands; (ii) addition of Kollman charges and polar hydrogens; (iii) generation of a docking grid box (dimensions: 40 Å × 40 Å × 40 Å, with a spacing of 0.375 Å) to encompass the active site [42].

For the ligands, the 3D structures of PDDA were designed and the energy minimized using Avogadro software [45]. Ciprofloxacin's 3D structure was retrieved from the PubChem database (Compound CID: 2764) and prepared for docking analysis. The interactions between the ligands (PDDA and ciprofloxacin) and the selected proteins (AgrA and LsrR) were analyzed using Discovery Studio [46] and visualized using PyMOL software [47].

Assessment of anti-quorum sensing activity

Anti-quorum sensing activity of PDDA was evaluated using the biosensor bacterial strain *Chromobacterium violaceum* CV026, and using a violacein inhibition assay previously reported [38]. CV026 was streaked onto Luria-Bertani (LB) agar and incubated at 30 °C for 24 h. A single colony was used to inoculate LB broth, which was incubated overnight at 30 °C. The resulting culture was adjusted to an OD_{600} of 1.2, and 5 mL of this suspension was incorporated into 25 mL of molten LB agar. To induce quorum sensing-dependent pigment production, N-hexanoyl homoserine lactone (C6-HSL) was added to the medium to a final concentration of 0.4 µg/mL. The mixture was gently homogenized, poured into sterile Petri dishes, and allowed to solidify at ambient temperature under aseptic conditions. After solidification, 6 mm diameter wells were formed using a sterile inverted Pasteur pipette. Each well was filled with 20 µL of PDDA at different concentration 1.56, 3.12, 6.25, 12.5, 25, and 50 µg/mL. A control plate was prepared by adding 100 µL of phosphate-buffered saline (PBS) to the medium instead of C6-HSL to serve as a negative control. All plates were incubated at 30 °C for 24 h. The absence or reduction of violacein pigmentation surrounding the wells containing PDDA indicated disruption of AHL-mediated signalling and thus quorum sensing. Experiments were conducted with two technical replicates per condition and three independent biological replicates.

Results and discussion

Synthesis and characterization of GO-PDDA-Ag nanocomposite

Figure 2 shows the UV-Vis spectra of GO, PDDA, AgNPs, and GO-PDDA-AgNP nanocomposites with distinct optical profiles. GO was characterized by two prominent features: a sharp peak at 230 nm, attributed to π-π* transitions of the aromatic C-C bonds, and a shoulder at 300 nm due to n-π* transitions of the C=O bonds, as previously reported [48]. PDDA exhibited a strong absorption peak at 230 nm, highlighting its unique optical properties [49]. The UV-Vis spectrum of the GO-PDDA-AgNP nanocomposite indicated the presence of AgNPs through the presence of a peak at approximately 420 nm. This peak was consistent with the outcome of previous studies, and corresponded to the surface plasmon resonance of AgNPs, confirming their small, spherical shape and effective distribution on GO [13, 50]. The UV-Vis spectra of the GO-PDDA*-Ag sample are provided in the Supplementary Information (Fig. SI3.c).

FTIR spectroscopy was conducted to analyse and identify the functional groups present in the nanomaterials and to investigate the interactions between GO and AgNPs. The results demonstrated that the FTIR spectrum of GO displayed several bands, including 1079 cm^{-1} (corresponding to alkoxy C-O), 1427 cm^{-1} (C–OH), 1627 cm^{-1} (C=C), 1731 cm^{-1} (C=O found in carboxylic acids and carbonyl groups), and 3405 cm^{-1} (–OH) (Fig. 3). These results are consistent with the main functional

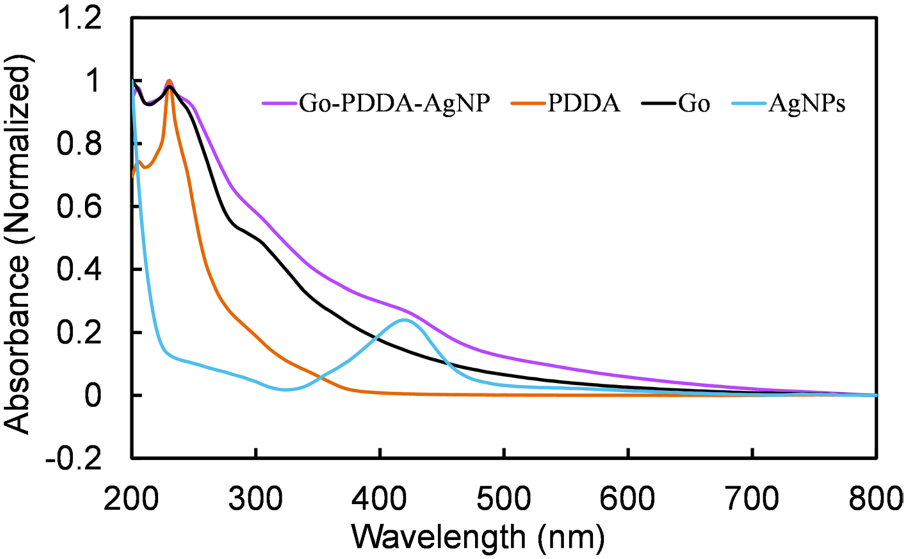

Fig. 2 **UV–vis spectra** of GO, Ag, and GO-PDDA-AgNP nanocomposites

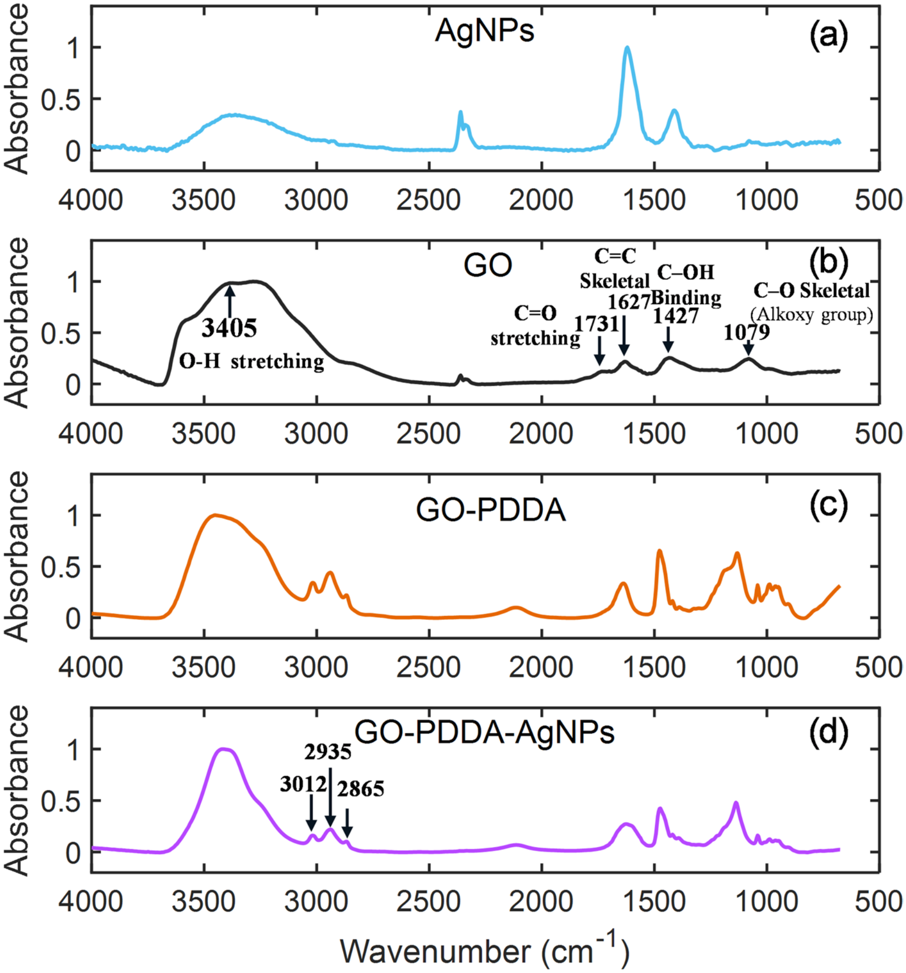

Fig. 3 **FTIR spectra**: (**a**) AgNPs and GO, (**b**) GO-PDDA, and GO-PDDA-AgNPS

groups previously identified in the structure of GO [51, 52]. The presence of oxygen-containing functional groups explains the excellent hydrophilicity of GO [53] and facilitates its modification with functional materials [54]. In addition to the previously mentioned bands, three new absorption bands were observed at approximately 2865, 2935 and 3012 cm^{-1} in the FTIR spectra of GO-PDDA. These bands indicate the functionalization of graphene oxide with PDDA. Compared to GO, the C=O (1731 cm^{-1}) vibration of −COOH was not observed for GO-PDDA and GO-PDDA-Ag, probably due to the bond between PDDA and −COOH of GO or the electrostatic interaction between AgNP and −COOH [55].

The FTIR analysis of GO-PDDA-AgNPs revealed a similar spectrum to GO-PDDA. However, the intensities of the absorption bands corresponding to the oxygen functional groups were lower. This change is explained by the linking of the AgNPs to the oxygen-containing functional groups (i.e., −COOH) that exist in the structure of GO most likely through the establishment of a chemical bond or electrostatic interaction, as has previously been reported [32, 50, 56]. The FTIR spectrum of GO-PDDA*-Ag is provided in the Supplementary Information (Fig. SI3.b), confirming the presence of the relevant functional groups, including the characteristic oxygen-containing bands discussed above.

Zeta potential measures the electrical potential at the slipping plane of nanoparticles in a colloidal system and is commonly used as an indicator of dispersion stability [57]. The zeta potential, particle size, and polydispersity index (PDI) for GO, AgNPs, GO-PDDA, and GO-PDDA-AgNPs are presented in Fig. 4. GO exhibited a strongly negative zeta potential (-40.5 mV), consistent with its surface oxygen-containing groups (e.g., carboxyl, epoxy, and hydroxyl), and an average particle size of 4057 nm (PDI: 0.18), likely reflecting sheet aggregation in suspensions. AgNPs displayed a smaller size (43.28 nm) with a zeta potential of -44 mV and a PDI of 0.35. After modification with the cationic polymer PDDA, GO-PDDA had a positive surface charge (+63.2 mV) and a reduced average size of 595 nm (PDI: 0.20), indicating improved dispersion. The GO-PDDA-AgNP nanocomposite retained a high positive surface charge (+57.5 mV) with a size of 491.4 nm and a PDI of 0.37, suggesting stable colloidal behaviour and successful PDDA-mediated assembly. These positive zeta potential values are indicative of strong electrostatic repulsion between particles, which enhances colloidal stability. A comparison of the obtained values with previously reported data is shown in Table 1. Consistent with previous studies, PDDA incorporation significantly shifted the zeta potential from negative to positive, enhancing both dispersion and potential adhesion to negatively charged bacterial membranes [58, 59].

The thermogravimetric profile in Fig. 5a displays the decomposition temperatures of GO-PDDA and GO-PDDA-Ag. The TGA curves of both samples exhibited

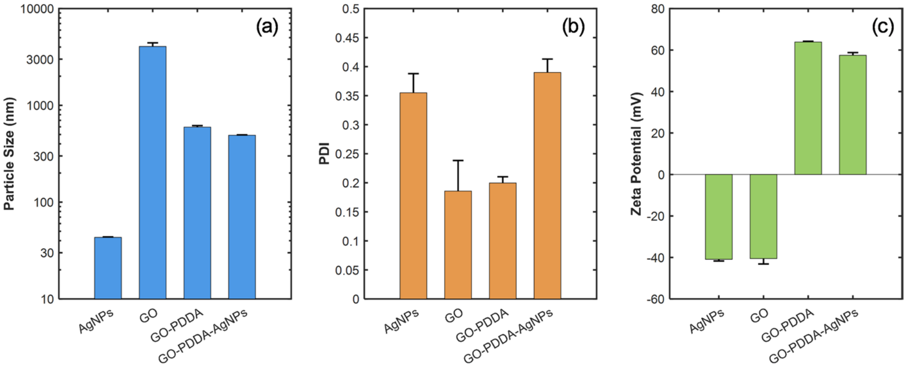

Fig. 4 **Stability analysis of GO, AgNPs, GO-PDDA, and GO-PDDA-AgNPs**: (**a**) Average particle size, showing the distribution and uniformity of particle size of GO, AgNPs, GO-PDDA, and GO-PDDA-AgNPs. (**b**) Polydispersity Index (PDI), indicating the uniformity of particle sizes, a lower PDI (close to 0) reflects a more monodispersed sample (**c**) Zeta potential values, representing the surface charge of each nanoparticle. GO exhibits a negative charge due to its functional groups, and the positive zeta potential of GO-PDDA and GO-PDDA-AgNPs is attributed to the cationic polymer PDDA. These zeta potential measurements provide insight into the colloidal stability of the nanoparticles, with higher absolute values indicating greater stability due to stronger electrostatic repulsion

Table 1 Comparison of the Zeta Potential of previously reported nanocomposites and the GO, AgNPs, GO-PDDA, and GO-PDDA-AgNPs prepared in the present study

Zeta Potentials (mV)								
Present study				Rongtao Zhao et al., 2018 [60]			Rongtao Zhao et al., 2017 [61]	
GO	GO-PDDA	AgNPs	GO-PDDA-AgNPs	GO	GO-AgNPs	GO-PEI-AgNPs	GO-Ag-NPs	GO-PEG-Ag-NPs
- 40.5	63.2	-44	57.5	−38	−38.4	45.8	- 38.4	16.2

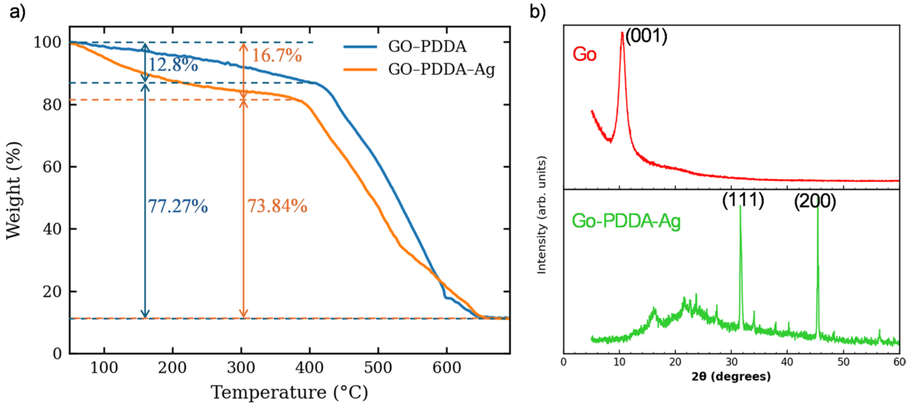

Fig. 5 (**a**) **TGA curves** of GO-PDDA and GO-PDDA-Ag. (**b**) XRD patterns of GO and GO-PDDA-Ag

two main mass-loss regions. In the first region, GO-PDDA showed a gradual weight loss of ~ 12.8% below ~420 °C, whereas GO-PDDA-Ag exhibited a slightly higher mass loss of ~ 16.7% below ~376 °C. This initial degradation can be linked to the elimination of physically adsorbed water, the removal of unstable oxygen-containing functional groups, and the partial breakdown of the PDDA side chains [62–64]. The second major mass-loss stage occurred between ~ 420 °C and ~ 650 °C, during which GO-PDDA and GO-PDDA-Ag lost approximately 77.27% and 73.84% of their mass, respectively. This pronounced decline could be linked to the pyrolytic decomposition of the PDDA backbone and the oxidation-driven degradation of the carbon framework [62, 63, 65]. Interestingly, the GO-PDDA-Ag nanocomposite presented a reduction in its thermal decomposition temperature, where the onset of major mass loss occurred earlier than in GO-PDDA. This behavior indicates that the presence of Ag nanoparticles facilitates decomposition, likely through enhanced heat transfer, leading to a lower temperature threshold for thermal degradation [66].

Figure 5b presents the XRD patterns of GO and the GO-PDDA-Ag nanocomposite. The diffractogram of GO (red curve) shows a strong peak at 2θ ≈ 10.4°, which corresponds to the (001) plane. In contrast, the GO–PDDA–Ag nanocomposite (green curve) displayed two sharp flections at 2θ ≈ 34° and 45°, assigned to the (111) and (200) crystallographic planes of metallic silver, which confirmed the anchoring of Ag nanoparticles within the GO–PDDA matrix [32, 67]. Additionally, a broad feature appeared in the 20–25° region, which was associated with the PDDA-coated graphene layers [68]. In contrast, the XRD pattern of the GO-PDDA*-AgNPs (Figure SI3-a) showed a noticeably weaker signal in the 20–25° region, consistent with the lower PDDA content in the GO-PDDA* formulation. Quantitative analysis by MP-AES (Agilent 4200) of the Ag remaining in the filtrate of the nanocomposite reaction made it possible to infer that the GO-PDDA-AgNP composite contained 5.22 µg/mL of silver. This analysis confirmed the successful incorporation of silver nanoparticles into the GO-PDDA matrix.

Antibacterial activity of synthesized nanocomposite GO-PDDA-AgNPs

The Disk Diffusion Method was employed to assess the antimicrobial activity of the individual components and fabricated test material (GO, AgNPs, PDDA, and GO-PDDA-AgNPs). In this method, a larger zone of bacterial growth inhibition was taken to indicate greater sensitivity of the test organism to the treatment, reflecting its effectiveness. Figures 6 and 7 present the inhibition zones obtained when 10 µl of the test materials, GO, PDDA, AgNPs, and GO-PDDA-AgNPs, were incubated with *E. coli* or *S. aureus*.

The disk diffusion results revealed that the GO-PDDA-AgNP nanocomposites exhibited notable antibacterial activity at all tested concentrations (10, 15, and 20 µg/mL) against the gram-positive bacteria *S. aureus*, producing inhibition zones of 8.5, 9.0, and 10.0 mm, respectively. This was indicated by the clear growth inhibition zone observed when the nanocomposite material was applied. No inhibition zones were detected for any of the test concentrations of the GO-PDDA-AgNP nanocomposite with the gram-negative bacteria, *E. coli*. Similarly, neither GO nor AgNPs alone provoked growth inhibition of *E. coli* or *S. aureus* at the concentrations tested (10, 15, and 20 µg/mL) (Fig. 6). It is worth noting that the concentrations of AgNPs (20 µg/mL) tested were higher than those present in the final nanocomposite for-

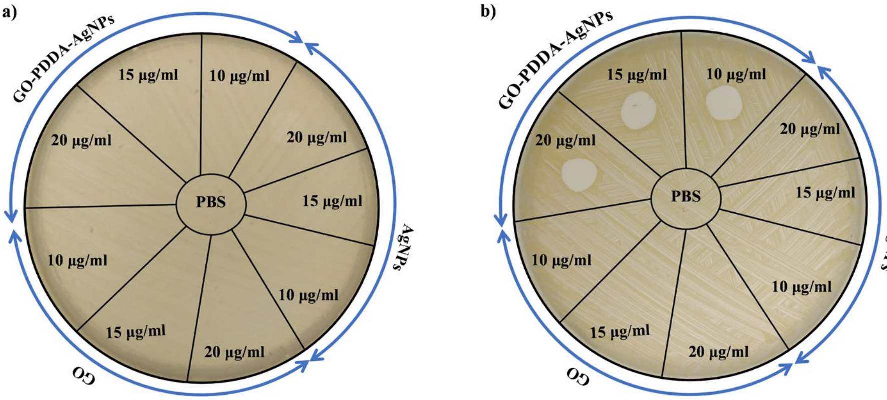

Fig. 6 Antibacterial activity of the synthesized nanocomposite GO-PDDA-AgNPs, GO, and AgNPs at concentrations of 10 µg/mL, 15 µg/mL, and 20 µg/mL against (**a**) *E. coli* and (**b**) *S. aureus*. The experiment was performed in triplicate on Mueller–Hinton agar medium at 37 °C and incubated for 24 h

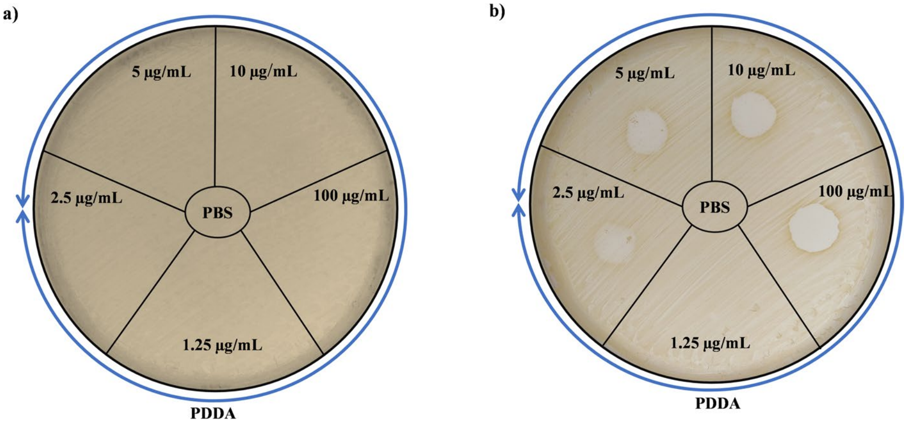

Fig. 7 Antibacterial activity of PDDA with serial dilutions (100 µg/mL, 10 µg/mL, 5 µg/mL, 2.5 µg/mL, and 1.25 µg/mL) against (**a**) *E. coli* and (**b**) *S. aureus*. The experiment was performed in triplicate on Mueller–Hinton agar medium at 37 °C and incubated for 24 h

mulation, while GO (4.0 mg/mL) was evaluated at the stock solution concentration (see Supplementary Material, Fig. SI4). The lack of anti-bacterial activity of GO and AgNPs likely reflects a combination of factors specific to the formulation and assay conditions used, including the relatively low AgNP dose, surface passivation by PDDA that limits Ag^+ release, and interactions with components of the MH medium that sequester silver ions or limit their and GO bioavailability and activity. These findings highlight that the antibacterial effects of GO and AgNPs are highly context-dependent, influenced by particle size, surface chemistry, concentration, medium composition, and exposure time [13, 69].

In contrast, serial dilutions (100 µg/mL, 10 µg/mL, 5 µg/mL and 2.5 µg/mL) of PDDA alone (Fig. 7b) were highly effective against *S. aureus*, producing inhibition zones of 11.5, 9.7, 9.5, and 6.0 mm, respectively, even at relatively low concentrations (5 µg/mL). At 2.5 µg/mL PDDA, the inhibition zone was weak, and the application site appeared slightly lighter, indicating limited antibacterial activity. It is worth noting that the PDDA concentration series tested was significantly lower than the concentrations used in the nanocomposite solution (around 1.02 mg/mL: 1 mL GO + 0.8 mL PDDA, followed by 150 µL GO–PDDA + 500 µL AgNPs). No inhibition zones were observed at any of the dilutions tested with *E. coli*, indicating that PDDA was ineffective (Fig. 7a) and that there was selective inhibition of *S. aureus* by PDDA.

The similarity of the antibacterial effect for both the GO–PDDA–AgNP nanocomposite and PDDA alone in the disk diffusion assay, and their consistent high positive surface charge suggests that the antimicrobial activity of the nanocomposite could be primarily attributable to PDDA. The high positive surface charge conferred by PDDA has been reported to promote strong electrostatic interactions with negatively charged bacterial membranes, ultimately leading to membrane disruption [70, 71]. In contrast, GO and AgNPs alone, have negative surface charges, and exhibited no inhibition zones, likely due to electrostatic repulsion that limited contact with bacterial membranes and therefore their antibacterial efficacy [72]. The selective activity of PDDA against *S. aureus*, but not *E. coli*, observed in the disk assay, was likely linked to the structural differences in the bacterial envelopes: Gram-positive bacteria like *S. aureus* lack the outer membrane that protects Gram-negative strains such as *E. coli*, making them more vulnerable to cationic agents [73, 74]. The increased susceptibility of *S. aureus* compared to *E. coli* in our study is consistent with findings with other similar nanocomposites. For instance, Bareke et al. (2024) demonstrated that a copper-based nanospinel ferrite (LiCu-F) completely inactivated *S. aureus*, while achieving only approximately 68% inhibition of *E. coli* under identical conditions [75]. Molecular docking analysis further indicated a stronger binding affinity of LiCu-F to a protein target in *S. aureus* than to a target in *E. coli* and was correlated with the experimentally observed Gram-specific antibacterial effect.

The heightened sensitivity of *S. aureus* to PDDA and the GO–PDDA–AgNP composite can be ascribed to molecular interactions with bacterial cell walls. The cationic groups of PDDA engage in electrostatic interactions with the negatively charged surface of Gram-positive bacteria, leading to membrane disruption and cell lysis [76]. Graphene oxide may further augment this effect by physically enveloping bacterial cells, while Ag^+ ions released from AgNPs generate reactive oxygen species (ROS) that inflict damage on cellular components [77, 78]. Collectively, these mechanisms may explain the pronounced antibacterial response in *S. aureus* and the diminished susceptibility of *E. coli*, that has an outer membrane that impedes such interactions. To further investigate the concentration dependence of PDDA's antimicrobial effect and define its minimum inhibitory concentration, bacterial growth curve assays were established across a dilution series. Bacterial growth curves were performed in the presence of PDDA (100 µg/mL, 10 µg/mL, 5 µg/mL, 2.5 µg/mL and 1.25 µg/mL) at lower concentrations than that used for the synthesis of the composite. The results are presented in Fig. 8 using OD_{600} to assess bacterial growth as a function of the incubation time. 100 µg/mL and 10 µg/mL concentrations of PDDA completely inhibited the growth of *S. aureus*, while for *E. coli* only the 100 µg/mL concentration of PDDA completely inhibited growth. To explore the relationship between PDDA concentration and its antibacterial activity, a nanocomposite was prepared using a highly diluted PDDA solution (1.25 µg/mL), a concentration that does not inhibit bacterial growth. This nanocomposite formulation, referred to as GO-PDDA*-AgNPs, exhib-

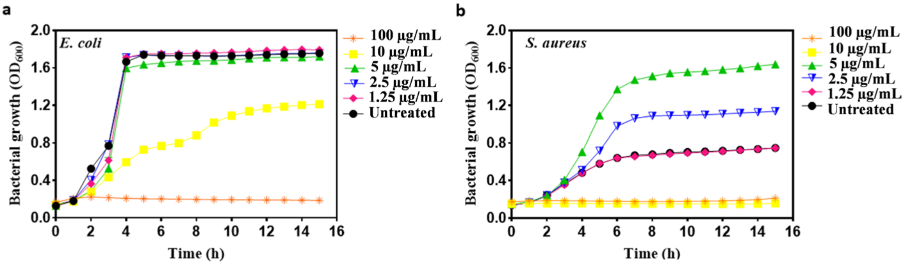

Fig. 8 **Growth curve** of *E. coli* (**a**) and *S. aureus* (**b**) after 24 h of treatment with different solutions from a serial dilution of PDDA (100 µg/mL, 10 µg/mL, 5 µg/mL, 2.5 µg/mL and 1.25 µg/mL). Bacterial growth kinetics were measured to evaluate the inhibitory effects of PDDA on both Gram-negative (*E. coli*) and Gram-positive (*S. aureus*) bacteria. The highest dilution of PDDA (1.25 µg/mL) did not have a significant inhibitory effect on bacterial growth for either *E. coli* or *S. aureus*

ited a negative surface charge and showed no antimicrobial effect against *S. aureus* or *E. coli* under the tested conditions. The growth kinetics and zeta potential data supporting these findings are provided in the Supplementary Information (Figures SI1 and SI2).

Whilst PDDA is identified as the primary driver of antibacterial activity in the GO-PDDA-AgNP composite, the GO/AgNP scaffold itself confers several functional advantages over free PDDA alone. First, PDDA functionalisation of GO dramatically improved colloidal stability, shifting the zeta potential from −40.5 mV (bare GO) to +57.5 mV in the final composite, confirming that PDDA is successfully oriented on the nanocomposite surface to maximise cationic charge exposure and enhance electrostatic interactions with negatively charged bacterial cell walls. This functionalisation also reduced the hydrodynamic size of GO from 4057 nm to 491.4 nm, ensuring that PDDA was maintained in a well-dispersed, functionally active state during in vitro assays. Furthermore, the GO-PDDA framework by modifying the well documented instability and spontaneous aggregation of AgNPs in aqueous environments, contributed to the preservation of their bioactive surface area, and explained their consistent antibacterial performance under the tested conditions.

Minimum inhibitory concentration of PDDA

The antibacterial efficacy of PDDA was further quantified utilizing a resazurin microdilution assay. As illustrated in Fig. 9, a concentration-dependent inhibition of bacterial growth was evident. The assay wells exhibiting bacterial growth demonstrated a color transition from blue to pink following incubation with resazurin, whereas wells that retained a blue color indicated the absence of bacterial proliferation. For *E. coli*, growth was observed at a PDDA concentration of 25 µg/mL but was absent at 50 µg/mL, placing the MIC between 25 and 50 µg/mL. For *S. aureus*, growth occurred at a PDDA concentration of 6.25 µg/mL but not at 12.5 µg/mL, placing the MIC between 6.25 and 12.5 µg/mL. Replating at the boundary concentrations confirmed these endpoints. No colonies were observed at 50 µg/mL for *E. coli* and 12.5 µg/mL for *S. aureus*, while growth was present at the next lower dilutions. Control wells containing MHB alone (sterility control) or MHB with PDDA but devoid of bacterial inoculum remained blue, confirming the absence of contamination and the non-interference of PDDA with the indicator dye. These findings indicate that PDDA possessed significant antibacterial activity against both Gram-negative and Gram-positive bacterial strains, and that *S. aureus* was most sensitive.

Impact of PDDA on *S. aureus* aggregation

Interestingly, at 5 µg/mL and 2.5 µg/mL PDDA, *S. aureus* cultures exhibited OD_{600} values higher than the untreated control (Fig. 8b). This unexpected increase is unlikely to reflect enhanced bacterial growth but rather suggests a physical effect such as cell aggregation and sedimentation, which can elevate turbidity readings. To further investigate this hypothesis, aggregation was evaluated through growth curve analysis, and by examining the morphology of PDDA-treated *S. aureus* by microscopy. As shown in Fig. 10a, the absorbance values of *S. aureus* after 14 h in the pres-

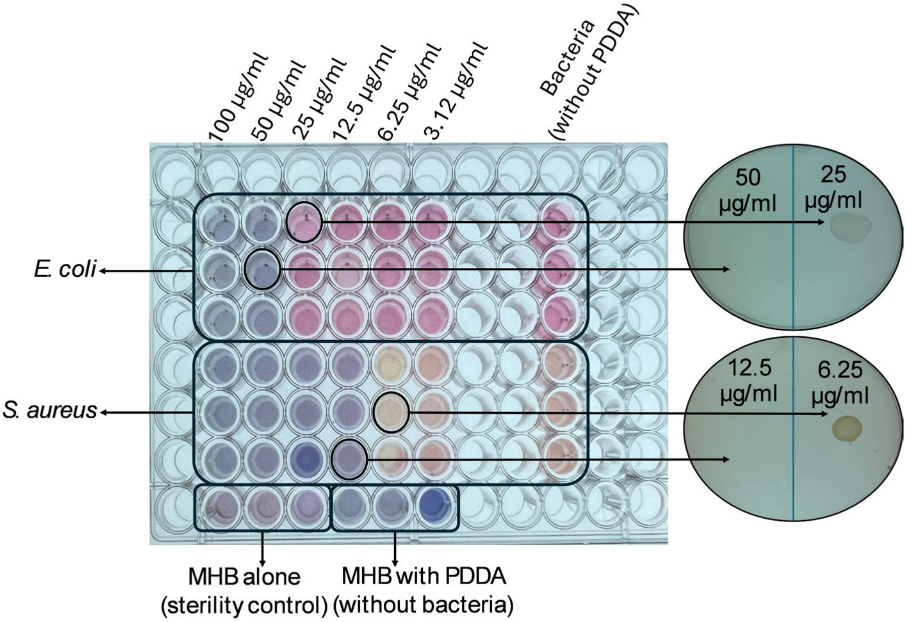

Fig. 9 **Resazurin microdilution MIC** and agar-spot confirmation of PDDA against *E. coli* and *S. aureus*. The 96-well microplate shows bacterial growth after exposure to PDDA (3.12–100 µg/mL); pink indicates growth and blue indicates growth inhibition. Controls include MHB and MHB + PDDA (no inoculum). Right, Petri dishes show replating from wells at 50, 25, 12.5, and 6.25 µg/mL to verify the first no-growth concentration (MIC)

ence of different PDDA concentrations, 5 µg/mL and 2.5 µg/mL, were significantly higher compared to the untreated *S. aureus* (Control). The increase in OD values at the 5 µg/mL and 2.5 µg/mL dilutions of PDDA after 14 h was caused by substantial bacterial aggregation and sedimentation to the bottom of the 96-well plates used for the assays (Fig. 10b). Bacterial aggregation started in the early exponential growth phase and may be due to electrostatic interactions facilitated by the cationic nature of PDDA, which caused the bacteria to cluster together. Examination of the bacteria by light microscopy (Fig. 10c) confirmed they were aggregated at concentrations of 5 µg/mL and 2.5 µg/mL of PDDA compared to the untreated controls. The results obtained with PDDA indicated it caused aggregation of *S. aureus*, which is consistent with previous studies showing that cationic polymers influence bacterial aggregation through electrostatic interactions [79]. Similar results were obtained by Zhang et al. (2017), who reported that the positively charged polymer PFP bound to negatively charged sites on the surface of *S. aureus* through electrostatic interactions [80]. In contrast, *E. coli* did not exhibit aggregation, likely due to its outer membrane acting as a barrier to such interactions.

The differential response of Gram-postive and Gram-negative bacteria can be explained by their distinct cell-wall architecture. *S. aureus*, like other Gram-positive bacterium, has a thick peptidoglycan layer (20–80 nm) that is densely cross-linked and predominantly negatively charged due to its contents of teichoic acid. This exposed anionic surface provides extensive electrostatic contact points for the cationic PDDA

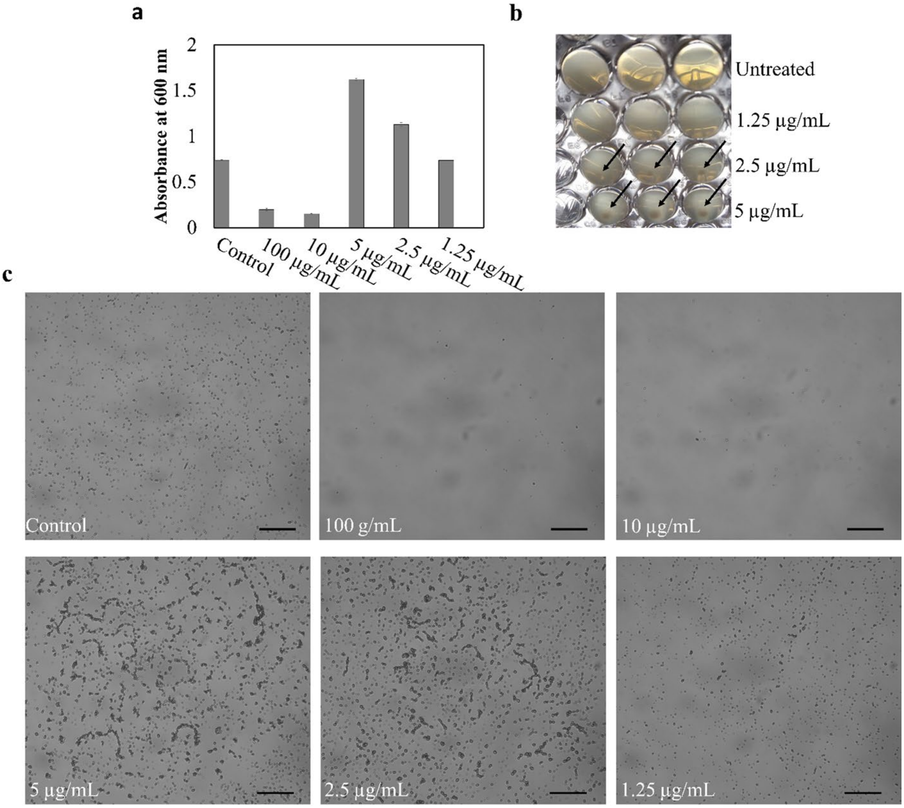

Fig. 10 Aggregation of *S. aureus* caused by PDDA: (**a**) Absorbance values of *S. aureus* after 14 h with different PDDA dilutions (100 µg/mL, 10 µg/mL, 5 µg/mL, 2.5 µg/mL and 1.25 µg/mL); (**b**) Visual observation of bacterial growth in 96-well plates at various PDDA dilutions, with the black arrows indicating the visible mass of aggregated bacteria. The increase in OD at the 2.5 µg/mL and 5 µg/mL PDDA dilutions is due to significant bacterial aggregation and sedimentation at the bottom of the wells; (**c**) Digital images captured from microscopy of untreated *S. aureus* cells (Control) and *S. aureus* cells incubated with serial dilutions of PDDA. Scale bars in the photographs represent 100 µm

polymer, facilitating strong binding, charge neutralisation, and subsequent bridging between adjacent cells to form aggregates [79, 80]. In contrast, *E. coli* has an outer membrane composed of lipopolysaccharide (LPS), which shields the thin underlying peptidoglycan layer (2–7 nm) from direct polymer contact. This hydrophobic and steric barrier limits the accessibility of PDDA to the inner cell wall, thereby reducing the extent of charge-mediated bridging and preventing visible aggregation at the concentrations tested. The structural differences in the outer membrane of bacteria provides a mechanistic basis explaining the PDDA-mediated aggregation of Gram-positive bacteria. Importantly, while aggregation was not observed in *E. coli* cultures, PDDA still exhibited moderate growth inhibition at higher concentrations (MIC 25–50 µg/mL), indicating that the outer membrane constitutes a partial, rather than absolute, barrier to PDDA's antibacterial action. This is consistent with the study of Louzao et al. [79], who showed that cationic polymers at sufficient concentration can disrupt bacterial cell envelopes even in Gram-negative species, albeit with lower efficiency than for Gram-positive organisms.

The results from both the growth inhibition and aggregation assays indicated that PDDA exhibited the highest antibacterial potency against *S. aureus* and also induced bacterial aggregation in *S. aureus* at sub-inhibitory concentrations. These findings suggest that PDDA may interact with *S. aureus* through a more specific mechanism than simple electrostatic disruption. To further explore this selective effect and gain molecular-level insights into PDDA's mode of action, docking simulations were performed targeting key quorum-sensing regulatory proteins: AgrA in *S. aureus* and LsrR in *E. coli*.

Molecular docking analysis

To investigate the interactions between PDDA and the bacterial proteins AgrA in *S. aureus* and LsrR in *E. coli*, molecular docking studies were performed. Ciprofloxacin, a well-known antibiotic, was included as a reference ligand to compare its binding interactions and affinities with those of PDDA. This comparison provided insight into the docking interactions of these compounds and clarified their potential antibacterial mechanisms. Table 2 summarizes the binding affinities and amino acid interactions of ciprofloxacin, PDDA with AgrA (from *S. aureus*) and LsrR (from *E. coli*).

Molecular docking results revealed that ciprofloxacin exhibited a stronger binding affinity towards AgrA in *S. aureus* (-5.37 kcal/mol) with residues Tyr 229, His 227, Glu 226, Phe 203, Gln 179, His 174, Lys 167, Ser 165, and Glu 163 (Fig. 11b). Additionally, it showed binding affinity towards LsrR in *E. coli* (-5.06 kcal/mol) with interactions involving residues Met 109, Val 87, Gln 85, Arg 79, and Glu 75, as shown in Table 2; Fig. 12b. The docking results aligned with those of Othman et al. (2023), in the interactions involving ciprofloxacin and the amino acids Tyr 229, His 227, Glu 226, and Glu 163 in the AgrA-binding pocket of *S. aureus*, as well as Met 109, Val 87, and Glu 75 in the LsrR protein of *E. coli* [42]. This consistency corroborates the validity of the docking approach and highlights the importance of these residues in the binding to AgrA and LsrR.

Molecular docking analysis revealed that PDDA exhibited strong binding affinities for AgrA (-5.11 kcal/mol) and LsrR (-3.76 kcal/mol), values that closely aligned

Table 2 Molecular docking scores and amino acid interactions of the bacterial proteins AgrA and LsrR with PDDA, and Ciprofloxacin

Organism	Bacterial protein	PDB ID	Ligand compound	Binding affinity (kcal/mol)	Interaction/Amino acids
S. aureus	AgrA	4G4K	PDDA	-5.11	Tyr229, His227, Glu226, Glu163
			Ciprofloxacin	−5.37	Tyr229, His227, Glu226, Phe203, Gln179, His174, Lys167, Ser165, Glu163
E. coli	LsrR	4L5J	PDDA	-3.76	Met109, Val89, Arg88, Val87, Glu75, Leu72
			Ciprofloxacin	-5.06	Met109, Val87, Gln85, Arg79, Glu75

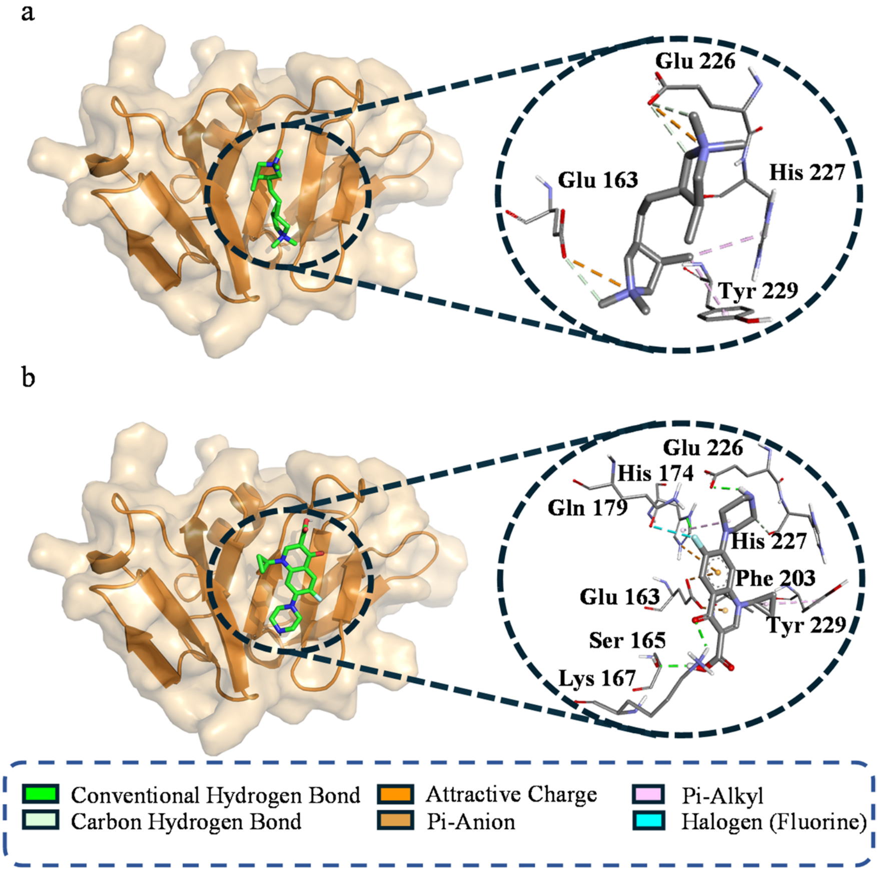

Fig. 11 **Molecular docking interactions** between *S. aureus* AgrA (PDB ID: 4G4K) and (**a**) PDDA, and (**b**) ciprofloxacin. The protein is represented as an orange surface model, with each docking pose displayed showing specific interactions in the zoomed-in insets. In (**a**), PDDA interacts with Glu 226, Glu 163, His 227, and Tyr 229. In (**b**), ciprofloxacin forms interactions with residues Glu 226, Gln 179, His 174, His 227, Glu 163, Ser 165, Lys 167, Phe 203, and Tyr 229

with the binding affinity of ciprofloxacin for these targets. In AgrA, PDDA formed electrostatic and hydrogen-bond interactions with Glu 163 and Glu 226, and π–alkyl interactions with Tyr 229 and His 227 (Fig. 11a). Importantly, Tyr 229 has been identified as a critical binding site for other AgrA inhibitors, such as bumetanide, which is known to inhibit AgrA through hydrogen bonding with this residue [81]. Additionally, the residue His 227 engages in hydrogen bonding with tryptophan, a molecule recognized for its antibiofilm properties [82].

In *E. coli*, PDDA formed electrostatic interactions with Glu 75 and Arg 88, carbon–hydrogen bonds with Val 87 and Val 89, and alkyl interactions with Met 109 and Leu 72 (Fig. 12a). The stronger binding of PDDA to AgrA relative to LsrR correlates with the observed in vitro antibacterial activity, indicating a more pronounced efficacy against *S. aureus*. The significant difference in binding strengths indicated that these QS proteins might contribute to the antibacterial effects of PDDA. Nonetheless,

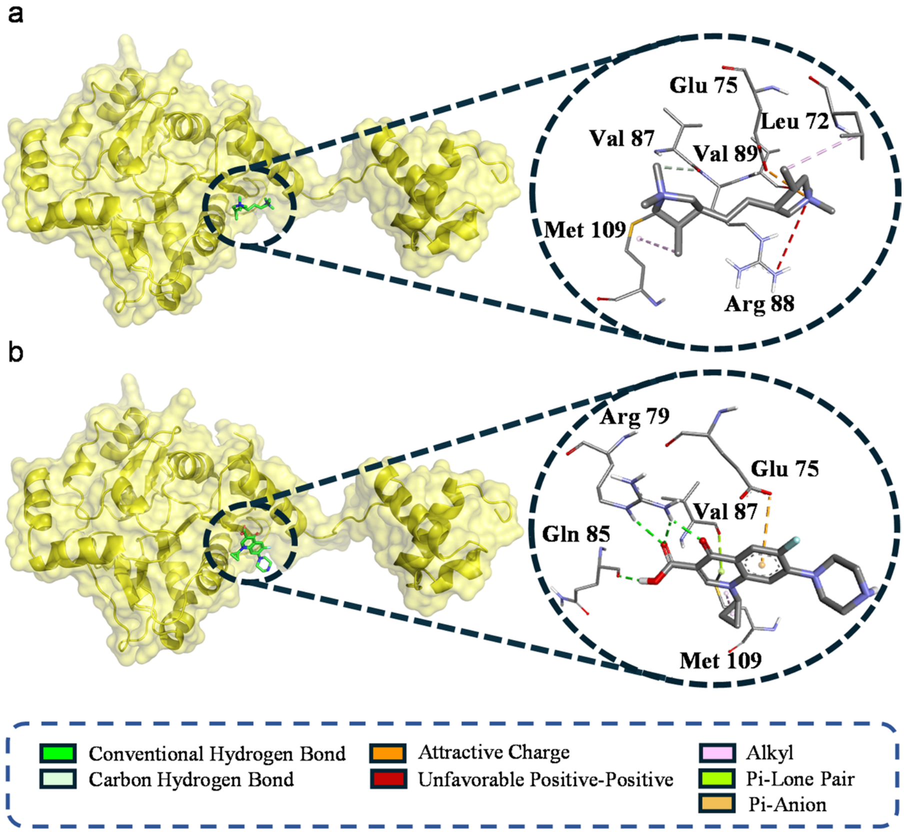

Fig. 12 **Molecular docking interactions** between *E. coli* LsrR (PDB ID: 4L5J) and (**a**) PDDA, (**b**) ciprofloxacin. The protein is represented as a yellow surface model, with each docking pose displayed to show specific interactions in the zoomed-in insets. In (**a**), PDDA forms key interactions with residues Glu 75, Val 87, Val 89, Leu 72, Arg 88, and Met 109. In (**b**), ciprofloxacin binds with Arg 79, Gln 85, Glu 75, Val 87, and Met 109.

other possible mechanisms, such as membrane disruption, or the production of ROS, cannot be excluded and might act synergistically. Additionally, although ciprofloxacin was used as a reference for docking, it was not experimentally tested in this study. However, as demonstrated by Othman et al. [42], ciprofloxacin can bind to various bacterial targets, including QS regulators like AgrA and LsrR, besides its known inhibition of DNA gyrase and topoisomerase IV. In this context, PDDA might have a similar function to antibiotics like ciprofloxacin, as supported by both the docking results and experimental evidence of their antibacterial properties.

The integration of experimental antibacterial assays and in silico docking studies aligns with recent research that combines these methodologies to elucidate mechanisms of action. Mustafa et al. (2023) developed a dual-function Mg-doped ferrite that achieved 83.8% degradation of 2,4,5-trichlorophenol while demonstrating potent bactericidal activity against *E. coli* and *S. aureus* [83]. Notably, they complemented their laboratory experiments with molecular docking simulations to elucidate the interaction between the nanoferrite and bacterial proteins, thereby providing molecular-level insights into its antimicrobial mechanism. Such studies highlight the potential of combining experimental and computational approaches to enhance mechanistic understanding of multifunctional nanomaterials. In a similar vein, our docking results, which indicated a higher affinity of PDDA for the *S. aureus* quorum-sensing protein, AgrA, compared to the quorum-sensing protein, LsrR, in *E. coli*, offer a plausible molecular explanation for the preferential antibacterial activity observed in vitro, although further validation is required.

Anti-quorum sensing activity

The anti-quorum sensing (AQS) properties of PDDA were evaluated in vitro using the biosensor *C. violaceum* CV026. This biosensor is a relevant tool for evaluating AQS activity, as it relies on the regulation of the characteristic water-insoluble pigment, violacein, via the LuxI/LuxR QS system [84]. However, the information provided by the assay depends on the context, and it was previously reported that although a gold (I) complex inhibited violacein production, it was unclear if this was due to true QS inhibition or simply a result of bacterial growth inhibition [38]. In the present study, PDDA was tested at concentrations ranging from 1.56 to 50 µg/mL, but none caused loss of the purple violacein colour (Figure SI4), indicating PDDA was not a QS system inhibitor in the *C. violaceum* CV026 biosensor (Figure SI4. b). However, it is important to note that the QS architecture of the Gram-negative *C. violaceum* (LuxI/LuxR-type system) is mechanistically distinct from the *agr* system of the Gram-positive *S. aureus* (AIP-mediated signalling via the AgrA response regulator). While the *C. violaceum* assay relies on the detection of acyl-homoserine lactones (AHLs), our docking studies focused specifically on the AgrA protein, which has no direct homolog in the *C. violaceum* pathway. Therefore, while PDDA does not appear to interfere with AHL-mediated signalling, the potential for interaction and action via the *S. aureus* AgrA protein remains a possibility that warrants further investigation in future studies.

Conclusion

In this study, a GO–PDDA–AgNP nanocomposite was synthesized, and the origin of its antibacterial activity was investigated. Physicochemical characterization (UV-Vis, FTIR, zeta potential) confirmed successful PDDA incorporation and the positive surface charge of the composite. Experimental findings suggested that the observed antimicrobial effects were predominantly associated with the presence of PDDA, which exhibited a strong electrostatic interaction with the negatively charged bacterial membranes. Notably, PDDA induced selective aggregation of *S. aureus* at sub-inhibitory concentrations and highlighted a strain-specific response. Based on these observations, a possible influence of PDDA's cationic nature on the QS systems was proposed. To explore this, molecular docking simulations were performed with PDDA and the QS regulatory proteins AgrA (*S. aureus*) and LsrR (*E. coli*), which indicated a higher predicted binding affinity to AgrA than to LsrR. Assessment in vitro of the anti-quorum sensing (AQS) properties of PDDA with the biosensor *C. violaceum* CV026 yielded inconclusive results and further experimental validation is required. While the findings clearly demonstrate PDDA's key role, likely via electrostatic interactions, in the nanocomposite's antibacterial activity, any specific QS-related mechanism remains speculative and requires experimental confirmation. This study underscores the need for rigorous evaluation of the functional contribution of each component in complex nanocomposites.

Supplementary Information The online version contains supplementary material available at https://doi.org/10.1007/s00289-026-06477-4.

Acknowledgements Thanks are extended to Dr. Leonor Faleiro for providing the bacterial strains used in this study, Dr. Anna Grenha for assistance with Zeta Potential measurements, and Dr. José Paulo Silva for assistance with the FTIR analysis. We also thank Dr. João Paulo Lourenço and Dr. Rui M. Borges dos Santos for coordinating access to the TGA and XRD facilities, Dr. Auguste Fernandes for performing the PXRD analysis, and Dr. Carlos E.S. Bernardes for the TGA analysis. This study received Portuguese national funds from FCT - Foundation for Science and Technology through project UIDB/04326/2020 (DOI:10.54499/ UIDB/04326/2020), UIDP/04326/2020 (DOI:10.54499/UIDP/04326/2020) and LA/P/0101/ 2020 (DOI:10.54499/LA/P/0101/2020), and from the operational programs CRESC Algarve 2020 and COMPETE 2020 through projects EMBRC.PT ALG-01-0145-FEDER-022121 and BIODATA.PT ALG-01-0145-FEDER-022231. Additional thanks are extended to the CNRST of Morocco and the Ministry of Higher Education in Morocco for their support of this work.

Author contributions Badr-Edine Sadoq: Writing – original draft, Methodology, Software, Visualization, Investigation, Formal analysis, Data curation, Conceptualization. **Youssef Elamine: ** Writing – original draft, Writing– review & editing, Validation, Supervision, Investigation, Formal analysis. **Inês Filipa Cabral Leal: ** Writing– review & editing, Methodology. **Adel Bouajaj: ** Writing– review & editing, Supervision, Funding acquisition. **Mohammed Reda Britel** : Writing– review & editing, Funding acquisition. **Amal Maurady: ** Supervision, Writing– review & editing, Methodology, Conceptualization, Formal analysis, Funding acquisition. **Deborah M. Power** : Writing – original draft, Writing – review & editing, Supervision, Formal analysis, Conceptualization, Project administration, Funding acquisition.

Funding Open access funding provided by FCT|FCCN (b-on).

Data availability Data sources were referenced in the methods, raw data is available for analysis on request.

Declarations

Competing interests The authors declare no competing interests.

References

1. Prakash J, Pivin JC, Swart HC (2015) Noble metal nanoparticles embedding into polymeric materials: From fundamentals to applications. Adv Colloid Interface Sci 226:187–202. https://doi.org/10.1016/j.cis.2015.10.010
2. Prakash J, Swart H (2023) Plasmonic photocatalysts as emerging multifunctional nanomaterials for energy and environmental applications. Phys B Condens Matter 669:415297. https://doi.org/10.1016/j.physb.2023.415297
3. Kumar V, Prakash J, Singh JP, Chae KH, Swart C, Ntwaeaborwa OM, Swart HC, Dutta V (2017) Role of silver doping on the defects related photoluminescence and antibacterial behaviour of zinc oxide nanoparticles. Colloids Surf B Biointerfaces 159:191–199. https://doi.org/10.1016/j.colsurfb.2017.07.071
4. Scott C, Wisdom NH, Coulter K, Bardin S, Strap JL, Trevani L (2023) Interdisciplinary Undergraduate Laboratory for an Integrated Chemistry/Biology Program: Synthesis of Silver Nanoparticles (AgNPs)-Cellulose Composite Materials with Antimicrobial Activity. J Chem Educ 100:1446–1454. https://doi.org/10.1021/acs.jchemed.2c00712
5. Kumar P, Chandra Mathpal M, Prakash J, Viljoen BC, Roos WD, Swart HC (2020) Band gap tailoring of cauliflower-shaped CuO nanostructures by Zn doping for antibacterial applications. J Alloys Compd 832:154968. https://doi.org/10.1016/j.jallcom.2020.154968
6. Rajamohan R, Ashokkumar S, Lee YR (2023) Environmental free synthesis of biologically active Cu2O nanoparticles for the cytotoxicity. J Mol Struct 1271:134081. https://doi.org/10.1016/j.molstruc.2022.134081
7. More PR, Pandit S, De Filippis A, Franci G, Mijakovic I, Galdiero M (2023) Silver Nanoparticles: Bactericidal and Mechanistic Approach against Drug Resistant Pathogens. Microorganisms 11:369. https://doi.org/10.3390/microorganisms11020369
8. Qi M, Wang X, Chen J, Liu Y, Liu Y, Jia J, Li L, Yue T, Gao L, Yan B, Zhao B, Xu M (2023) Transformation, Absorption and Toxicological Mechanisms of Silver Nanoparticles in the Gastrointestinal Tract Following Oral Exposure. ACS Nano 17:8851–8865. https://doi.org/10.1021/acsnano.3c00024
9. Menichetti A, Mavridi-Printezi A, Mordini D, Montalti M (2023) Effect of Size, Shape and Surface Functionalization on the Antibacterial Activity of Silver Nanoparticles. J Funct Biomater 14. https://doi.org/10.3390/jfb14050244
10. Goharshadi EK, Goharshadi K, Moghayedi M (2022) The use of nanotechnology in the fight against viruses: A critical review. Coord Chem Rev 464:214559. https://doi.org/10.1016/j.ccr.2022.214559
11. El-Zahed MM, Abou-Dobara MI, El-Khodary MM, Mousa MMA (2024) Antimicrobial activity and nanoremediation of heavy metals using biosynthesized CS/GO/ZnO nanocomposite by Bacillus subtilis ATCC 6633 alone or immobilized in a macroporous cryogel, Microb. Cell Fact 23:278. https://doi.org/10.1186/s12934-024-02535-6
12. Morones JR, Elechiguerra JL, Camacho A, Holt K, Kouri JB, Ramírez JT, Yacaman MJ (2005) The bactericidal effect of silver nanoparticles. Nanotechnology 16:2346–2353. https://doi.org/10.1088/0957-4484/16/10/059
13. Cobos M, De-La-Pinta I, Quindós G, Fernández MJ, Fernández MD (2020) Graphene Oxide–Silver Nanoparticle Nanohybrids: Synthesis, Characterization, and Antimicrobial Properties. Nanomaterials 10:376. https://doi.org/10.3390/nano10020376
14. Kumar P, Huo P, Zhang R, Liu B (2019) Antibacterial properties of graphene-based nanomaterials. Nanomaterials 9:1–32. https://doi.org/10.3390/nano9050737
15. Avcu E, Bastan FE, Guney M, Yildiran Avcu Y, Ur Rehman MA, Boccaccini AR (2022) Biodegradable Polymer Matrix Composites Containing Graphene-Related Materials for Antibacterial Applications: A Critical Review, Acta Biomater. 151:1–44. https://doi.org/10.1016/j.actbio.2022.07.048
16. Tan S, Wu X, Xing Y, Lilak S, Wu M, Zhao JX (2020) Enhanced synergetic antibacterial activity by a reduce graphene oxide/Ag nanocomposite through the photothermal effect, Colloids Surf. B Biointerfaces 185:110616. https://doi.org/10.1016/j.colsurfb.2019.110616
17. Moghayedi M, Goharshadi EK, Ghazvini K, Ahmadzadeh H, Jorabchi MN (2020) Antibacterial activity of Ag nanoparticles/phosphomolybdate/reduced graphene oxide nanocomposite: Kinetics and mechanism insights. Mater Sci Engineering: B 262:114709. https://doi.org/10.1016/j.mseb.2020.114709

18. El-Zahed MM, Baka ZA, Abou-Dobara MI, El-Sayed AK, Aboser MM, Hyder A (2021) In vivo toxicity and antitumor activity of newly green synthesized reduced graphene oxide/silver nanocomposites. Bioresour Bioprocess 8:44. https://doi.org/10.1186/s40643-021-00400-7
19. El-Zahed MM, Baka ZAM, El-Sayed AKA, Abou-Dobara MI (2022) The anti-aspergillus potential of optimized biosynthesized reduced graphene oxide/silver nanocomposite using Escherichia coli D8 (MF062579. J Microbiol Biotechnol Food Sci e5864. https://doi.org/10.55251/jmbfs.5864
20. Sharifi M, Marjani A, Mahdavian L, Shamlouei HR (2023) Computational Study on Production Mechanism of Nano-Graphene Oxide/Poly Diallyl Dimethyl Ammonium Chloride (NGO/PDADMAC) Nanocomposite, Polycycl. Aromat Compd 43:1158–1171. https://doi.org/10.1080/10406638.2022.2025867
21. Lu J, Wang X, Xiao C (2008) Preparation and characterization of konjac glucomannan/poly(diallydimethylammonium chloride) antibacterial blend films. Carbohydr Polym 73:427–437. https://doi.org/10.1016/j.carbpol.2007.12.021
22. Veerakumar P, Sangili A, Chen SM, Lin KC (2020) Ultrafine gold nanoparticle embedded poly(diallyldimethylammonium chloride)-graphene oxide hydrogels for voltammetric determination of an antimicrobial drug (metronidazole). J Mater Chem C Mater 8:7575–7590. https://doi.org/10.1039/c9tc06690j
23. Wang C, Guo R, Lan J, Tan L, Jiang S, Xiang C (2018) Preparation of multi-functional fabric via silver/reduced graphene oxide coating with poly(diallyldimethylammonium chloride) modification. J Mater Sci: Mater Electron 29:8010–8019. https://doi.org/10.1007/s10854-018-8807-8
24. Goharshadi EK, Azizi-Toupkanloo H (2013) Silver colloid nanoparticles: Ultrasound-assisted synthesis, electrical and rheological properties. Powder Technol 237:97–101. https://doi.org/10.1016/j.powtec.2012.12.059
25. Du T, Lu J, Liu L, Dong N, Fang L, Xiao S, Han H (2018) Antiviral Activity of Graphene Oxide-Silver Nanocomposites by Preventing Viral Entry and Activation of the Antiviral Innate Immune Response, ACS Appl. Bio Mater 1:1286–1293. https://doi.org/10.1021/acsabm.8b00154
26. Ma L, Zhu Z, Su M, Ma L, Liu D, Wang Z (2013) Preparation of graphene oxide-silver nanoparticle nanohybrids with highly antibacterial capability. Talanta 117. https://doi.org/10.1016/j.talanta.2013.09.017
27. Zhang S, Shao Y, Yin G, Lin Y (2009) Stabilization of platinum nanoparticle electrocatalysts for oxygen reduction using poly(diallyldimethylammonium chloride). J Mater Chem 19:7995. https://doi.org/10.1039/b912104h
28. Jang S-C, Kang S-M, Kim GY, Rethinasabapathy M, Haldorai Y, Lee I, Han Y-K, Renshaw JC, Roh C, Huh YS (2018) Versatile Poly(Diallyl Dimethyl Ammonium Chloride)-Layered Nanocomposites for Removal of Cesium in Water Purification. Materials 11:998. https://doi.org/10.3390/ma11060998
29. Sanches LM, Petri DFS, de Melo Carrasco LD, Carmona-Ribeiro AM (2015) The antimicrobial activity of free and immobilized poly (diallyldimethylammonium) chloride in nanoparticles of poly (methylmethacrylate). J Nanobiotechnol 13:58. https://doi.org/10.1186/s12951-015-0123-3
30. Yu Y, Chen Z, He S, Zhang B, Li X, Yao M (2014) Direct electron transfer of glucose oxidase and biosensing for glucose based on PDDA-capped gold nanoparticle modified graphene/multi-walled carbon nanotubes electrode. Biosens Bioelectron 52:147–152. https://doi.org/10.1016/j.bios.2013.08.043
31. Zhang A, Fan Y, Wang N, Yu H (2025) A sensitive bromate sensor based on a gold nanoparticle-poly(diallyldimethylammonium chloride)–reduced graphene oxide nanocomposite modified glassy carbon electrode. Microchim Acta 192:43. https://doi.org/10.1007/s00604-024-06871-7
32. Shen J, Li T, Shi M, Li N, Ye M (2012) Polyelectrolyte-assisted one-step hydrothermal synthesis of Ag-reduced graphene oxide composite and its antibacterial properties. Mater Sci Engineering: C 32:2042–2047. https://doi.org/10.1016/j.msec.2012.05.017
33. Kar A, Mukherjee SK, Barik S, Hossain ST (2024) Antimicrobial Activity of Trigonelline Hydrochloride Against Pseudomonas aeruginosa and Its Quorum-Sensing Regulated Molecular Mechanisms on Biofilm Formation and Virulence. ACS Infect Dis 10:746–762. https://doi.org/10.1021/acsinfecdis.3c00617
34. Zou Y, Liu C, Zhang H, Wu Y, Lin Y, Cheng J, Lu K, Li L, Zhang Y, Chen H, Yu Q (2022) Three lines of defense: A multifunctional coating with anti-adhesion, bacteria-killing and anti-quorum sensing properties for preventing biofilm formation of Pseudomonas aeruginosa. Acta Biomater 151:254–263. https://doi.org/10.1016/j.actbio.2022.08.008

35. Sionov RV, Steinberg D (2022) Targeting the Holy Triangle of Quorum Sensing, Biofilm Formation, and Antibiotic Resistance in Pathogenic Bacteria. Microorganisms 10:1239. https://doi.org/10.3390/microorganisms10061239
36. Sadoq B-E, Mujwar S, Sadoq M, Boulaamane Y, Britel MR, Bouajaj A, Touhami A, Touhami F, Maurady A (2025) Metal and Metal Oxide Nanoparticles: Computational Analysis of Their Interactions and Antibacterial Activities Against Pseudomonas aeruginosa. Bionanoscience 15:60. https://doi.org/10.1007/s12668-024-01625-4
37. Lee LC, Liong C-Y, Jemain AA (2017) A contemporary review on Data Preprocessing (DP) practice strategy in ATR-FTIR spectrum. Chemometr Intell Lab Syst 163:64–75. https://doi.org/10.1016/j.chemolab.2017.02.008
38. Marques A, Carabineiro SAC, Aureliano M, Faleiro L (2023) Evaluation of Gold Complexes to Address Bacterial Resistance, Quorum Sensing, Biofilm Formation, and Their Antiviral Properties against Bacteriophages. Toxics 11:879. https://doi.org/10.3390/toxics11110879
39. Zhong C, Zajki-Zechmeister K, Nidetzky B (2021) Reducing end thiol-modified nanocellulose: Bottom-up enzymatic synthesis and use for templated assembly of silver nanoparticles into biocidal composite material. Carbohydr Polym 260:117772. https://doi.org/10.1016/j.carbpol.2021.117772
40. Sarker SD, Nahar L, Kumarasamy Y (2007) Microtitre plate-based antibacterial assay incorporating resazurin as an indicator of cell growth, and its application in the in vitro antibacterial screening of phytochemicals. Methods 42:321–324. https://doi.org/10.1016/j.ymeth.2007.01.006
41. Saha S, Ghosh M (2024) Computational exploration of natural compounds targeting Staphylococcus aureus: inhibiting AgrA promoter binding for antimicrobial intervention. J Biomol Struct Dyn 42:8256–8267. https://doi.org/10.1080/07391102.2023.2246566
42. Othman AS, Shamekh IM, Abdalla M, Eltayb WA, Ahmed NA (2023) Molecular modeling study of micro and nanocurcumin with in vitro and in vivo antibacterial validation. Sci Rep 13:12224. https://doi.org/10.1038/s41598-023-38652-2
43. Morris GM, Huey R, Lindstrom W, Sanner MF, Belew RK, Goodsell DS, Olson AJ (2009) AutoDock4 and AutoDockTools4: Automated docking with selective receptor flexibility. Wiley Online Libr 30:2785–2791. https://doi.org/10.1002/jcc.21256
44. Chalkha M, Nour H, Chebbac K, Nakkabi A, Bahsis L, Bakhouch M, Akhazzane M, Bourass M, Chtita S, Bin Jardan YA, Augustyniak M, Bourhia M, Aboul-Soud MAM, El Yazidi M (2022) Synthesis, Characterization, DFT Mechanistic Study, Antimicrobial Activity, Molecular Modeling, and ADMET Properties of Novel Pyrazole-isoxazoline Hybrids. ACS Omega 7:46731–46744. https://doi.org/10.1021/acsomega.2c05788
45. Hanwell MD, Curtis DE, Lonie DC, Vandermeerschd T, Zurek E, Hutchison GR (2012) Avogadro: An advanced semantic chemical editor, visualization, and analysis platform. J Cheminform 4. https://doi.org/10.1186/1758-2946-4-17
46. Pawar SS, Rohane SH (2021) Review on Discovery Studio: An important Tool for Molecular Docking. Asian J Res Chem 14:1–3. https://doi.org/10.5958/0974-4150.2021.00014.6
47. Yuan S, Chan HCS, Hu Z (2017) Using PyMOL as a platform for computational drug design. WIREs Comput Mol Sci 7:1–10. https://doi.org/10.1002/wcms.1298
48. Tang J, Chen Q, Xu L, Zhang S, Feng L, Cheng L, Xu H, Liu Z, Peng R (2013) Graphene oxide-silver nanocomposite as a highly effective antibacterial agent with species-specific mechanisms. ACS Appl Mater Interfaces 5:3867–3874. https://doi.org/10.1021/AM4005495
49. Fan Y, Zhao Y, Chen D, Wang X, Peng X, Tian J (2015) Synthesis of Pd nanoparticles supported on PDDA functionalized graphene for ethanol electro-oxidation. Int J Hydrogen Energy 40:322–329. https://doi.org/10.1016/j.ijhydene.2014.10.115
50. Hui KS, Hui KN, Dinh DA, Tsang CH, Cho YR, Zhou W, Hong X, Chun HH (2014) Green synthesis of dimension-controlled silver nanoparticle-graphene oxide with in situ ultrasonication. Acta Mater 64:326–332. https://doi.org/10.1016/j.actamat.2013.10.045
51. Tu TH, Cam PTN, Huy LVT, Phong MT, Nam HM, Hieu NH (2019) Synthesis and application of graphene oxide aerogel as an adsorbent for removal of dyes from water. Mater Lett 238:134–137. https://doi.org/10.1016/j.matlet.2018.11.164
52. Trang NTT, Thy LTM, Cuong PM, Tu TH, Hieu NH (2018) Fabrication and characterization of akaganeite/graphene oxide nanocomposite for arsenic removal from water, in: AIP Conf. Proc., : p. 040001. https://doi.org/10.1063/1.5033401
53. Liu S, Zeng TH, Hofmann M, Burcombe E, Wei J, Jiang R, Kong J, Chen Y (2011) Antibacterial activity of graphite, graphite oxide, graphene oxide, and reduced graphene oxide: membrane and oxidative stress. ACS Publications 5:6971–6980. https://doi.org/10.1021/nn202451x

54. Zou X, Zhang L, Wang Z, Luo Y (2016) Mechanisms of the Antimicrobial Activities of Graphene Materials. J Am Chem Soc 138:2064–2077. https://doi.org/10.1021/JACS.5B11411
55. Shao W, Liu X, Min H, Dong G, Feng Q, Zuo S (2015) Preparation, Characterization, and Antibacterial Activity of Silver Nanoparticle-Decorated Graphene Oxide Nanocomposite. ACS Appl Mater Interfaces 7:6966–6973. https://doi.org/10.1021/acsami.5b00937
56. Bao Q, Zhang D, Qi P (2011) Synthesis and characterization of silver nanoparticle and graphene oxide nanosheet composites as a bactericidal agent for water disinfection. J Colloid Interface Sci 360:463–470. https://doi.org/10.1016/j.jcis.2011.05.009
57. Sahu D, Sahoo G, Mohapatra P, Swain SK (2019) Dual Activities of Nano Silver Embedded Reduced Graphene Oxide Using Clove Leaf Extracts: Hg2 + Sensing and Catalytic Degradation, ChemistrySelect 4 2593–2602. https://doi.org/10.1002/slct.201803725
58. Mariadoss AVA, Ramachandran V, Shalini V, Agilan B, Franklin JH, Sanjay K, Alaa YG, Tawfiq MAA, Ernest D (2019) Green synthesis, characterization and antibacterial activity of silver nanoparticles by Malus domestica and its cytotoxic effect on (MCF-7) cell line. Microb Pathog 135. https://doi.org/10.1016/j.micpath.2019.103609
59. Hemlata PR, Meena AP, Singh KK, Tejavath (2020) Biosynthesis of Silver Nanoparticles Using Cucumis prophetarum Aqueous Leaf Extract and Their Antibacterial and Antiproliferative Activity against Cancer Cell Lines. ACS Omega 5:5520–5528. https://doi.org/10.1021/acsomega.0c00155
60. Zhao R, Kong W, Sun M, Yang Y, Liu W, Lv M, Song S, Wang L, Song H, Hao R (2018) Highly Stable Graphene-Based Nanocomposite (GO-PEI-Ag) with Broad-Spectrum, Long-Term Antimicrobial Activity and Antibiofilm Effects. ACS Appl Mater Interfaces 10:17617–17629. https://doi.org/10.1021/acsami.8b03185
61. Zhao R, Lv M, Li Y, Sun M, Kong W, Wang L, Song S, Fan C, Jia L, Qiu S, Sun Y, Song H, Hao R (2017) Stable Nanocomposite Based on PEGylated and Silver Nanoparticles Loaded Graphene Oxide for Long-Term Antibacterial Activity. ACS Appl Mater Interfaces 9:15328–15341. https://doi.org/10.1021/acsami.7b03987
62. Farivar F, Lay Yap P, Karunagaran RU, Losic D (2021) Thermogravimetric Analysis (TGA) of Graphene Materials: Effect of Particle Size of Graphene, Graphene Oxide and Graphite on Thermal Parameters, C (Basel). 7:41. https://doi.org/10.3390/c7020041
63. Yap PL, Kabiri S, Tran DNH, Losic D (2019) Multifunctional Binding Chemistry on Modified Graphene Composite for Selective and Highly Efficient Adsorption of Mercury. ACS Appl Mater Interfaces 11:6350–6362. https://doi.org/10.1021/acsami.8b17131
64. Jia X, Zhan X, Xie J, Gao B, Zhang Y (2020) Thermal stability of poly(diallyldimethylammonium chloride) with different molecular weight. J Macromolecular Sci Part A 57:83–90. https://doi.org/10.1080/10601325.2019.1671771
65. Fang Y, Guo S, Zhu C, Zhai Y, Wang E (2010) Self-Assembly of Cationic Polyelectrolyte-Functionalized Graphene Nanosheets and Gold Nanoparticles: A Two-Dimensional Heterostructure for Hydrogen Peroxide Sensing. Langmuir 26:11277–11282. https://doi.org/10.1021/la100575g
66. de Moraes ACM, Araujo Lima B, Fonseca de Faria A, Brocchi M, Luiz O, Alves (2015) Graphene oxide-silver nanocomposite as a promising biocidal agent against methicillin-resistant Staphylococcus aureus. Int J Nanomed 10:6847. https://doi.org/10.2147/IJN.S90660
67. Luz EPCG, da Silva TF, Marques LSM, Andrade A, Lorevice MVV, Andrade FK, Yang L, de Souza Filho AG, Faria AF (2024) Silveira Vieira, Bacteria-Derived Cellulose Membranes Modified with Graphene Oxide-Silver Nanoparticles for Accelerating Wound Healing, ACS Appl. Bio Mater 7:5530–5540. https://doi.org/10.1021/acsabm.4c00650
68. Saha A, Basiruddin S, Ray SC, Roy SS, Jana NR (2010) Functionalized graphene and graphene oxide solution via polyacrylate coating. Nanoscale 2:2777. https://doi.org/10.1039/c0nr00376j
69. Lange A, Sawosz E, Wierzbicki M, Kutwin M, Daniluk K, Strojny B, Ostrowska A, Wójcik B, Łojkowski M, Gołębiewski M, Chwalibog A, Jaworski S (2022) Nanocomposites of Graphene Oxide—Silver Nanoparticles for Enhanced Antibacterial Activity: Mechanism of Action and Medical Textiles Coating. Materials 15:3122. https://doi.org/10.3390/ma15093122
70. Radovic-Moreno AF, Lu TK, Puscasu VA, Yoon CJ, Langer R, Farokhzad OC (2012) Surface charge-switching polymeric nanoparticles for bacterial cell wall-targeted delivery of antibiotics. ACS Nano 6:4279–4287. https://doi.org/10.1021/nn3008383
71. Chen J, Wang F, Liu Q, Du J (2014) Antibacterial polymeric nanostructures for biomedical applications. Chem Commun 50:14482–14493. https://doi.org/10.1039/C4CC03001J

72. Magdalane CM, Kaviyarasu K, Vijaya JJ, Siddhardha B, Jeyaraj B (2016) Photocatalytic activity of binary metal oxide nanocomposites of CeO2/CdO nanospheres: Investigation of optical and antimicrobial activity. J Photochem Photobiol B 163:77–86. https://doi.org/10.1016/j.jphotobiol.2016.08.013
73. MacDonald TJ, Wu K, Sehmi SK, Noimark S, Peveler WJ, Du Toit H, Voelcker NH, Allan E, MacRobert AJ, Gavriilidis A, Parkin IP (2016) Thiol-Capped Gold Nanoparticles Swell-Encapsulated into Polyurethane as Powerful Antibacterial Surfaces under Dark and Light Conditions. Sci Rep 6:1–11. https://doi.org/10.1038/srep39272
74. Guo C, Nolan EM (2024) Exploring the Antibacterial Activity and Cellular Fates of Enterobactin-Drug Conjugates That Target Gram-Negative Bacterial Pathogens. Acc Chem Res 57:1046–1056. https://doi.org/10.1021/acs.accounts.3c00814
75. Bareke H, Oladipo AA (2024) Antimicrobial activity of biogenic-synthesized novel bimetallic nanospinel LiCu-ferrite particles: Experimental and computational studies. J Mol Struct 1296:136823. https://doi.org/10.1016/j.molstruc.2023.136823
76. Zuo Y, Kwok RTK, Sun J, Lam JWY, Tang BZ (2023) Aggregation-Induced Emission Macromolecular Materials for Antibacterial Applications. Wiley Online Libr 44. https://doi.org/10.1002/MARC.202300104
77. Ravikumar V, Mijakovic I, Pandit S (2022) Antimicrobial Activity of Graphene Oxide Contributes to Alteration of Key Stress-Related and Membrane Bound Proteins. Int J Nanomed Volume 17:6707–6721. https://doi.org/10.2147/IJN.S387590
78. Park H-J, Kim JY, Kim J, Lee J-H, Hahn J-S, Gu MB, Yoon J (2009) Silver-ion-mediated reactive oxygen species generation affecting bactericidal activity. Water Res 43:1027–1032. https://doi.org/10.1016/j.watres.2008.12.002
79. Louzao I, Sui C, Winzer K, Fernandez-Trillo F, Alexander C (2015) Cationic polymer mediated bacterial clustering: Cell-adhesive properties of homo- and copolymers. Eur J Pharm Biopharm 95:47–62. https://doi.org/10.1016/j.ejpb.2015.05.026
80. Zhang P, Li S, Chen H, Wang X, Liu L, Lv F, Wang S (2017) Biofilm Inhibition and Elimination Regulated by Cationic Conjugated Polymers. ACS Appl Mater Interfaces 9:16933–16938. https://doi.org/10.1021/acsami.7b05227
81. Palaniappan B, Solomon AP, C DR (2021) Targeting AgrA quorum sensing regulator by bumetanide attenuates virulence in Staphylococcus aureus – A drug repurposing approach. Life Sci 273:119306. https://doi.org/10.1016/j.lfs.2021.119306
82. Paul P, Chakraborty P, Sarker RK, Chatterjee A, Maiti D, Das A, Mandal S, Bhattacharjee S, Dastidar DG, Tribedi P (2021) Tryptophan interferes with the quorum sensing and cell surface hydrophobicity of Staphylococcus aureus: a promising approach to inhibit the biofilm development, 3 Biotech 11. 376. https://doi.org/10.1007/s13205-021-02924-3
83. Mustafa FS, Oladipo AA (2023) Dual function Mg-doped binary metal ferrite: Photocatalytic degradation of trichlorophenol, bactericidal activity and molecular docking analysis. Chemosphere 312:137348. https://doi.org/10.1016/j.chemosphere.2022.137348
84. McClean KH, Winson MK, Fish L, Taylor A, Chhabra SR, Camara M, Daykin M, Lamb JH, Swift S, Bycroft BW, Stewart GSAB, Williams P (1997) Quorum sensing and Chromobacterium violaceum: exploitation of violacein production and inhibition for the detection of N-acylhomoserine lactones, Microbiology (N. Y). 143:3703–3711. https://doi.org/10.1099/00221287-143-12-3703

Authors and Affiliations

Badr-Edine Sadoq[1,3] · Youssef Elamine[2] · Inês Filipa Cabral Leal[3] · Adel Bouajaj[1] · Mohammed Reda Britel[1] · Amal Maurady[1,4] · Deborah M. Power[3,5]

✉ Amal Maurady
amaurady@uae.ac.ma

✉ Deborah M. Power
dpower@ualg.pt

[1] Laboratory of Innovative Technologies, National School of Applied Sciences of Tangier, Abdelmalek Essaadi University, Tetouan, Morocco

[2] Instituto de Telecomunicações, Departamento de Engenharia Electrotécnica e de Computadores, Universidade de Coimbra, Coimbra 3030-290, Portugal

[3] Centro de Ciências do Mar do Algarve (CCMAR), Campus de Gambelas, Universidade do Algarve, 8005-139 Faro, Portugal

[4] Faculty of Sciences and Techniques of Tangier, Abdelmalek Essaadi University, Tetouan, Morocco

[5] International Research Center for Marine Biosciences (Ministry of Science and Technology), Shanghai Ocean University, Shanghai, China